Implementation of a GPU-enhanced multiclass soil erosion model based on the 2D shallow water equations in the software Iber

Luis Cea[1], Orlando García-Feal[1,2], Guillaume Nord[3], Guillaume Piton[3], Cédric Legoût[3]

[1]Universidade da Coruña, Water and Environmental Engineering Group, Center for Technological Innovation in Construction and Civil Engineering (CITEEC), Campus de Elviña, 15071 A Coruña, Spain

[2]Centro de Investigación Mariña, Universidade de Vigo, Environmental Physics Laboratory (CIM-EPhysLab), Campus Auga, 32004 Ourense, Spain

[3]Univ. Grenoble Alpes, INRAE, CNRS, IRD, Grenoble INP, IGE, 38000 Grenoble, France.

Key Points:

- A module computing multiclass soil erosion and sediment transport is implemented in a 2D shallow water hydrodynamic model
- Solid transport due to bed load and suspended load are modelled considering rainfall and runoff driven detachment processes
- The model is parallelized for GPUs enabling its application to complex catchments and river networks

Corresponding author: Luis Cea, `luis.cea@udc.es`

Abstract

Physically-based soil erosion models are valuable tools for the understanding and efficient management of soil erosion related problems at the basin and river reach scales, as soil loss, muddy floods, freshwater pollution or reservoir siltation, among others. We present the implementation of a new fully distributed multiclass soil erosion module. The model is based on a 2D finite volume solver (Iber+) for the 2D shallow water equations that computes the overland flow water depths and velocities. From these, the model evaluates the transport of sediment particles due to bed load and suspended load, including rainfall-driven and runoff-driven erosion processes, and using well-established physically-based formulations. The evolution of the mass of sediment particles in the soil layer is computed from a mass conservation equation for each sediment class. The solver is implemented using High Performance Computing techniques that take advantage of the computational capabilities of standard Graphical Processing Units, achieving speed-ups of two orders of magnitude relative to a sequential implementation on the CPU. We show the application and validation of the model at different spatial scales, ranging from laboratory experiments to meso-scale catchments.

1 Introduction

Soil erosion and sediment transport involve complex processes at different spatial and temporal scales, including the detachment of soil particles, the transport and redistribution of these particles by the overland flow, and eventually their deposition in regions different from where they were eroded. A correct understanding of the role of these processes at the basin and river reach scales is needed for an efficient management of soil erosion related problems as soil loss, muddy floods, freshwater pollution or reservoir siltation, among others.

Physically-based distributed soil erosion models can contribute to the understanding and interpretation of laboratory and *in-situ* measurements and therefore, to the analysis of the processes involved in soil erosion. Once calibrated with and validated with experimental or field data, a numerical model can be used to complement the available observations, and to validate or propose new hypothesis.

Several recent studies have shown that, with a proper calibration of bed friction and infiltration, and a well-defined Digital Terrain Model (DTM), the 2D Shallow Wa-

ter Equations (2D-SWE) are able to correctly reproduce water depths, velocities, and discharges under surface runoff conditions (Cea et al., 2014; Mügler et al., 2011; Tatard et al., 2008), and are therefore a good basis for physically-based soil erosion models. At the same time, several physically-based formulations that represent these processes at their lowest scales have been proposed and tested in laboratory and field experiments (Beuselinck et al., 1999, 2002; Foster et al., 1995; Govers, 1992; Hairsine & Rose, 1992a, 1992b; Jomaa et al., 2010; Kinnell, 1990, 2005; Nord & Esteves, 2007; Shaw et al., 2006, 2009), and have been shown to be a good basis to be implemented in a distributed erosion model (Cea et al., 2016; Heng et al., 2011; Nord & Esteves, 2005, 2007; Tromp-van Meerveld et al., 2008; Ouyang et al., 2023). In order to take advantage of their full potential these formulations require a detailed definition of the sediment properties, as well as an accurate spatial characterisation of the flow field, and therefore of the topography, land use, rainfall intensity and infiltration.

This paper presents an event-scale two-dimensional soil erosion and sediment transport model that can be applied from the plot or reach scale to the catchment scale. The model is implemented in the software Iber (Bladé et al., 2014), which computes the overland flow velocities and water depths from the 2D-SWE, including rainfall and infiltration terms. Soil erosion is computed using physically-based formulations, considering multiple sediment classes that might be transported either as suspended load or as bed load. A 2D transport equation is solved for each sediment class, considering the processes of rainfall and flow detachment, convective transport and deposition of sediment particles. Changes in the topography are computed from the 2D Exner equation, and considered in the hydrodynamic equations in order to couple the sediment transport with the overland flow. The hydrodynamic equations, as well as the sediment transport and Exner equations are solved with a GPU-enhanced finite volume solver, taking advantage of High Performance Computing (HPC) techniques and achieving speed-ups up to two orders of magnitude. This is essential in order to solve the equations with a high spatial and temporal resolution, while keeping computational times relatively low. Thus, the tool presented makes it possible to compute and analyse sediment transport processes at multiple locations and scales as plots on hillslopes, river reaches and catchments, by solving physically-based equations with a temporal and spatial resolution much higher than standard soil erosion models.

The paper is organised as follows. Section 2 describes the soil erosion processes included in the model and their mathematical representation. Section 3 presents the numerical schemes used to solve the model equations, as well as the High Performance Computing implementation that makes use of the computational capabilities of Graphical Processing Units (GPU). Section 4 presents four test cases that cover different potential applications of the model, including the calibration and validation of the model with observed data at the laboratory scale and at the field scale. Section 5 summarises the main conclusions, capabilities and limitations of the model.

2 MODEL EQUATIONS

This section presents the mathematical equations solved by the soil erosion model. The overland flow equations are presented briefly, since they are well-known and have already been discussed and validated for river and surface runoff applications in many previous studies. The soil erosion equations are presented in more detail, since their implementation differs from other soil erosion models, specially at the hillslope and catchment scales.

2.1 Hydrodynamic equations

The overland flow water depths and velocities are computed from the hydrodynamic module of the software Iber, which solves the 2D-SWE including rainfall and infiltration terms (Bladé et al., 2014; Cea & Bladé, 2015):

$$\frac{\partial h}{\partial t} + \frac{\partial q_x}{\partial x} + \frac{\partial q_y}{\partial y} = r - f \tag{1}$$

$$\frac{\partial q_x}{\partial t} + \frac{\partial}{\partial x}\left(\frac{q_x^2}{h} + \frac{gh^2}{2}\right) + \frac{\partial}{\partial y}\left(\frac{q_x q_y}{h}\right) = -gh\frac{\partial z_b}{\partial x} - ghI_x \tag{2}$$

$$\frac{\partial q_y}{\partial t} + \frac{\partial}{\partial x}\left(\frac{q_x q_y}{h}\right) + \frac{\partial}{\partial y}\left(\frac{q_y^2}{h} + \frac{gh^2}{2}\right) = -gh\frac{\partial z_b}{\partial y} - ghI_y \tag{3}$$

where x and y are the two horizontal directions, t is the time, z_b is the bed elevation, h is the water depth, (q_x, q_y) are the two components of the unit discharge in the two horizontal directions, (I_x, I_y) are the two components of the bed friction slope, g is the gravity acceleration, r is the rainfall rate and f is the infiltration rate. The two components of the depth averaged water velocity (U_x, U_y) are computed as the ratio between the corresponding unit discharges and the water depth. The bed friction slope can be

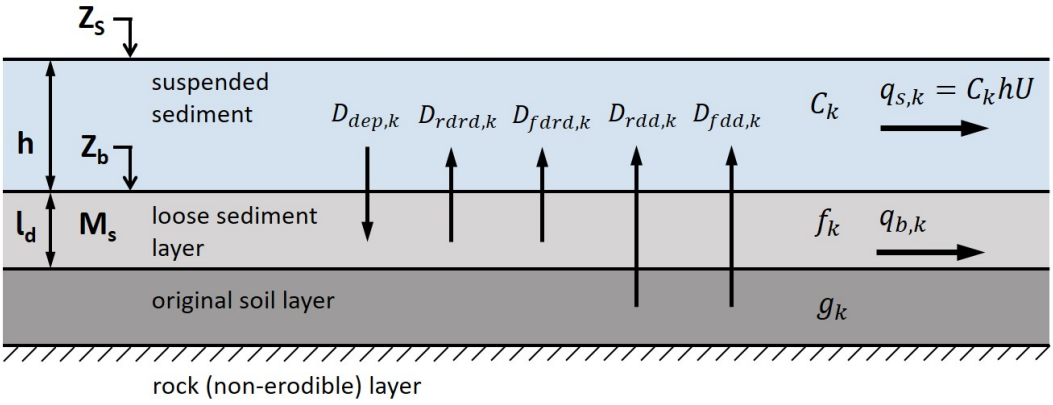

Figure 1. Vertical structure of the soil and components of the soil erosion model.

computed with any empirical formulation, as those of Manning, Chezy or Keulegan. In all the case studies presented in this work the formulation of Manning was used.

2.2 Soil erosion conceptual model

The soil erosion model considers that the sediment is formed by a mixture of N_p particle classes with a different characteristic diameter (D_k, with $k = 1, N_p$). The vertical structure of the soil is represented as a layer of loose sediment (low cohesion) lying over a layer of original soil matrix (Figure 1). Below the original soil layer lies a non-erodible rock layer that limits the maximum soil erosion. The mass fraction of each particle class in the loose sediment and original soil layers might be different and is represented by f_k and g_k respectively in Figure 1. The size distribution of sediment in the original soil layer (g_k) is defined by the user as input data, with the only restriction that the sum of the mass fractions for all classes must be equal to 1 (i.e., $\sum g_k = 1$). On the other hand, the spatial and temporal evolution of the mass fractions in the loose sediment layer (f_k) is computed by the model, ensuring also that the sum over all fractions is equal to one ($\sum f_k = 1$). The initial mass of each particle class in the loose sediment layer must also be defined by the user as an initial condition, and might vary in space.

The total mass of sediment per unit surface in the loose sediment layer (M_s) and its thickness (l_d) are related by:

$$l_d = \frac{M_s}{\rho_s \phi} \tag{4}$$

where ρ_s is the mass density of the solid particles and ϕ is the porosity of the soil layer. From Equation (4), an equivalent thickness for each sediment fraction ($l_{d,k}$) in the loose sediment layer can be defined as (assuming that all sediment classes have the same mass density):

$$l_{d,k} = \frac{l_d}{M_s} M_{s,k} = \frac{M_{s,k}}{\rho_s \phi} \tag{5}$$

where $M_{s,k}$ is the mass per unit surface of sediment class k in the loose sediment layer.

Two modes of transport are considered for each sediment class: bed load and suspended load ($q_{b,k}$ and $q_{s,k}$ respectively in Figure 1). Suspended load takes place over the whole water column, assuming that the sediment particles move with the depth-averaged water velocity (same modulus and direction). The depth-averaged suspended sediment concentration for each class (C_k) is computed from a mass conservation equation that considers the detachment of sediment from both, the loose sediment and the original soil layers, as well as the deposition of sediment in the eroded layer, as it will be detailed in the following section.

Bed load takes place in the upper part of the loose sediment layer and therefore, it is subject to the availability of sediment in that layer. The movement of particles that are transported as bed load is computed from a standard empirical bed load formulation, as detailed in section 2.4.

All the mathematical equations used to represent the previous processes are described in the following.

2.3 Suspended load

Suspended load for sediment class k is computed as $q_{s,k} = C_k |U| h$, where $|U|$ is the modulus of the depth-averaged velocity and C_k is the depth-averaged suspended sediment concentration of class k. The temporal and spatial evolution of the concentration for each sediment class is computed from the following depth-averaged scalar transport equation:

$$\frac{\partial h C_k}{\partial t} + \frac{\partial q_x C_k}{\partial x} + \frac{\partial q_y C_k}{\partial y} = D_{rdd,k} + D_{rdrd,k} + D_{fdd,k} + D_{fdrd,k} + D_{dep,k} \tag{6}$$

where $D_{rdd,k}$ and $D_{fdd,k}$ are the rainfall-driven and flow-driven detachment rates of sediment class k from the original soil layer, $D_{rdrd,k}$ and $D_{fdrd,k}$ are the rainfall-driven and flow-driven redetachment rates of sediment class k from the loose sediment layer, and

141 $D_{dep,k}$ is the deposition rate of sediment class k from the water column into the loose
142 sediment layer (Figure 1). All the source terms in Equation (6) are expressed in kg/m^2/s.
143 The model can also consider the horizontal mass transfer due to turbulent diffusion, but
144 the related terms are not included in Equation (6) for the sake of conciseness, since in
145 the applications presented in this work its influence is negligible with respect to the other
146 terms in the equation.

147 If the rainfall and flow driven redetachment rates are larger than the deposition rate
148 (i.e. $D_{rdrd,k} + D_{fdrd,k} > D_{dep,k}$), there is a net transfer of sediment particles of class
149 k from the loose sediment layer to the water column. Conversely, if deposition overcomes
150 the sum of both redetachment rates, the mass of sediment class k in the loose sediment
151 layer will increase.

The rainfall driven detachment and redetachment rates are calculated assuming a linear relation with the rainfall intensity (Li, 1979; Sharma et al., 1993, 1995; Gao et al., 2003) as:

$$D_{rdd,k} = \alpha_{d,k} r \left(1 - \varepsilon\right) f_d g_k \qquad D_{rdrd,k} = \alpha_{rd,k} r \varepsilon f_d f_k \tag{7}$$

with:

$$f_d = \left(\frac{z_m}{\max(h, z_m)}\right)^{0.8} \qquad \varepsilon = \min\left(\frac{M_s}{M_{s,cr}}, 1\right) \tag{8}$$

152 where the rainfall rate r is given in m/s, $\alpha_{d,k}$ and $\alpha_{rd,k}$ (kg/m/m^2) are the rainfall erodi-
153 bility coefficients for each particle class in the original soil matrix and in the loose sed-
154 iment layer respectively, ε is a shield factor that represents the protection effect that the
155 loose sediment layer exerts over the original soil layer, and f_d is a rainfall damping fac-
156 tor that accounts for the dissipation of rainfall energy through the water column (Hong
157 et al., 2016; Naves et al., 2020).

158 The shield factor ε is assumed to vary linearly between 0 and 1 with the total mass
159 of sediment per unit surface in the loose sediment layer (M_s), and it takes the same value
160 for all the particle classes (Figure 2). When M_s achieves a critical threshold ($M_{s,cr}$) the
161 protection effect is maximum ($\varepsilon = 1$), and no sediment is eroded from the original soil
162 matrix (i.e. $D_{rdd,k} = D_{fdd,k} = 0$).

163 The rainfall damping factor f_d also varies between 0 and 1 (Figure 2). If the wa-
164 ter depth is smaller than a given user-defined threshold (z_m) there is no rainfall damp-
165 ing (i.e. $f_d = 1$ if $h \leq z_m$). For larger depths it decreases exponentially with the wa-
166 ter depth (Figure 2).

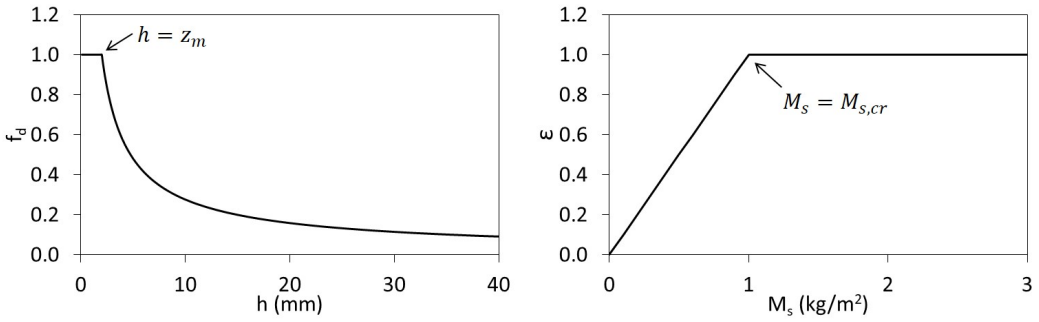

Figure 2. Rainfall damping factor (left) and shield factor (right) used to compute the rainfall driven detachment and redetachment rates.

167 This kind of formulations for rainfall driven erosion, with slightly different imple-
168 mentations of the rainfall damping factor, have been used in previous studies (Cea et al.,
169 2016; Gao et al., 2003; Naves et al., 2020; Nord & Esteves, 2005; Sharma et al., 1995;
170 Shaw et al., 2006; Uber et al., 2021).

The flow driven detachment rate represents the transfer of sediment particles from the original soil matrix to the water column due to bed shear stress, and it is computed for each sediment class as (Foster et al., 1995):

$$D_{fdd,k} = K_{d,k} \max\left(\tau - \tau_s, 0\right)\left(1 - \varepsilon\right) g_k \tag{9}$$

171 where $K_{d,k}$ is the flow driven detachability for each particle class expressed in kg/s/N,
172 τ is the bed shear stress and τ_s is the critical bed shear stress of the original soil matrix.
173 The flow driven detachability and the critical bed shear stress are model parameters to
174 be defined by the user, while the bed friction is computed with an empirical formulation
175 (e.g. Manning) when solving the 2D-SWE. The flow driven detachment is also modu-
176 lated by ε and g_k, similarly to the rainfall driven detachment.

The flow driven redetachment of sediment particles from the loose sediment layer into the water column is modelled with Hairsine formulation as (Hairsine & Rose, 1992a, 1992b):

$$D_{fdrd,k} = \frac{\rho_s F_k}{\left(\rho_s - \rho\right) g}\left(\frac{\Omega - \Omega_0}{h}\right)\varepsilon f_k \tag{10}$$

177 where Ω is the stream power of the flow expressed in W/m^2, Ω_0 is the critical stream
178 power below which the redetachment rate is zero, and F_k is the fraction of stream power
179 used for the redetachment of particles from the loose sediment layer into the water col-
180 umn.

Finally, the deposition of suspended sediment into the eroded layer is modelled as:

$$D_{dep,k} = -\rho_s w_{s,k} C_k \tag{11}$$

where $w_{s,k}$ is the effective settling velocity of the sediment particles of class k. Several formulations can be used to compute the settling velocity of a spherical particle in still water as a function of its density and diameter. We have used for that purpose the formulation of van Rijn (van Rijn, 1984).

$$w_{s,k} = \begin{cases} \dfrac{RgD_k^2}{18\nu} & \text{if} \quad D_k \leq 10^{-4}m \\ \dfrac{10\nu}{D_k}\left(\sqrt{1+\dfrac{RgD_k^3}{100\nu^2}}-1\right) & \text{if} \quad 10^{-4}m < D_k \leq 10^{-3}m \\ 1.1\sqrt{RgD_k} & \text{if} \quad 10^{-3}m < D_k \end{cases} \tag{12}$$

However, in practical applications the water is not still, and the sediment particles can interact with each other, both factors affecting their settling velocity. Thus, the effective settling velocity depends on the suspended sediment concentration, floculation, turbulence intensity and infiltration rate through the soil, and might even be used as a calibration parameter (Tromp-van Meerveld et al., 2008).

2.4 Bed load

The bed load transport capacity for each particle class ($q_{b,k}$ expressed in m^2/s) is computed as:

$$q_{b,k} = q^*_{b,k}\sqrt{\frac{\rho_s - \rho}{\rho} g D_k^3}\varepsilon f_k \tag{13}$$

where $q^*_{b,k}$ is the dimensionless bed load transport capacity, which can be computed with any empirical formulation. The following well-known formulations are implemented in the model: Meyer Peter-Müller, Wong-Parker, Einstein-Brown, van Rijn, Engelund-Hansen, Yalin and Ashida-Michiue (Garcia, 2006).

Most of these empirical formulations include a critical shear stress that depends on the particle diameter, and might therefore have a different value for each sediment class. Moreover, its value depends on the presence of other particle classes in the mixture. This interaction between particles of different size is considered in the model as (Garcia, 2006):

$$\tau_{c,k} = \tau_c \frac{D_k}{D_m}^{1-\gamma} \tag{14}$$

where $\tau_{c,k}$ is the critical shear stress of particle class k, τ_c is the critical shear stress corresponding to the mean diameter of the mixture, D_m is the mean diameter of the mixture and γ is the so-called *hiding factor*, which varies between 0 and 1, and controls the interaction between particles of different size. If $\gamma = 1$, the critical shear stress takes the same value for all sediment classes (i.e. there is a maximum interaction or hiding). A value of $\gamma = 0$ recovers the no-interaction hypothesis, in which case the critical shear stress varies linearly with the particle diameter.

2.5 Soil erosion

Once the suspended load and bed load are computed, the following mass conservation equation is solved to compute the time evolution of each particle class in the loose sediment layer:

$$\frac{\partial M_{s,k}}{\partial t} = -\left(D_{rdrd,k} + D_{fdrd,k} + D_{dep,k}\right) - \rho_s \left(\frac{\partial q_{bx,k}}{\partial x} + \frac{\partial q_{by,k}}{\partial y}\right) \tag{15}$$

Notice that only the terms involving the transfer of sediment from or to the loose sediment layer (Figure 1) are considered in Equation (15). The total mass of sediment and the mass fraction of sediment particle class are updated as:

$$M_s = \sum_{k=1}^{N_p} M_{s,k} \qquad\qquad f_k = \frac{M_{s,k}}{M_s} \tag{16}$$

Lastly, the evolution of the bed elevation is computed from the following mass conservation equation, which includes all the terms implying transfers of sediment particles from or to the loose sediment layer and the original soil layer:

$$\begin{aligned} \frac{\partial z_b}{\partial t} &= -\sum_{k=1}^{N_p} \frac{D_{rdd,k} + D_{rdrd,k} + D_{fdd,k} + D_{fdrd,k} + D_{dep,k}}{(1-\phi)\,\rho_s} \\ &- \sum_{k=1}^{N_p} \frac{1}{(1-\phi)} \left(\frac{\partial q_{bx,k}}{\partial x} + \frac{\partial q_{by,k}}{\partial y}\right) \end{aligned} \tag{17}$$

At each time step the new bed elevation computed from Equation (17) is updated in the 2D-SWE to ensure an appropriate coupling between the overland flow and soil erosion.

2.6 External forcings and boundary conditions

The hydrodynamic and soil erosion equations must be provided with appropriate boundary conditions and external forcings in order to be solved.

In rainfall-runoff applications at the catchment or at the hillslope scales, rainfall intensity is the main external forcing and might be provided by the user either as spatially variable raster fields for each time step, or as time series at specific rain gauge locations. In both cases the rainfall is interpolated to the elements of the computational mesh, providing a temporally and spatially variable rainfall field that is included as a source term in the mass conservation equation (source term r in Equation (1)), and used to compute the rainfall driven detachment and redetachment rates in the suspended sediment transport equation (source terms D_{rdd} and D_{rdrd} in Equation (7)).

When applying the model at the river reach scale, the main forcings are the inlet discharges of water and sediment at the upstream boundary. The inlet hydrograph and sedigraph (or alternatively the depth-averaged sediment concentration) along the upstream boundary must be provided by the user. Doing the approximation that the friction slope is uniform along the inlet boundary, the total discharge is distributed along the inlet length as:

$$q_{bnd} = K\frac{h^{5/3}}{n} \qquad K = \frac{Q_{in}}{\int\limits_{\Gamma_{bnd}} \frac{h^{5/3}}{n} dL} \tag{18}$$

where q_{bnd} is the unit discharge along the inlet boundary, Q_{in} is the total inlet discharge through that boundary, Γ_{bnd} is the contour of the inlet boundary, and n is the Manning coefficient along the boundary.

At the outlet boundaries only the water depth must be prescribed. This can be done either as a user-defined water level or as a supercritical flow condition. The former one is applied when the flow at the boundary is subcritical, while the latter one is appropriate when the boundary flow is supercritical. Typically, in mild slope reaches the water level at the outlet boundary is prescribed, while for steep slope river reaches, or at the catchment and hillslope scales, a supercritical flow condition is in general more convenient.

3 NUMERICAL SOLVER

3.1 Numerical schemes

The 2D-SWE (equations (1-3)), as well as the sediment transport equations (6), (15) and (17) are solved with a finite volume solver for unstructured grids. Numerical details of the finite volume method applied to the 2D-SWE and other transport equa-

tions are extensively described in the scientific literature. The reader is referred to LeVeque (2002); Toro (2001, 2009) and the references therein.

In the solver presented here two different numerical schemes were implemented for the discretisation of the convective terms in the 2D-SWE: a Godunov-type scheme based on the approximate Riemman solver of Roe (Toro, 2001) and the DHD scheme (Cea & Bladé, 2015). Numerical details about the specific implementation of the solver of Roe used in this work can be found in (Cea et al., 2010), while the description and validation of the DHD scheme is presented in (Cea & Bladé, 2015). Even if both schemes can be used to solve the 2D-SWE, the scheme of Roe is more efficient and accurate in the presence of shock waves, providing accurate and stable results at the river reach scale (Cea et al., 2007; Echeverribar et al., 2019), while the DHD scheme provides more stable and rapid results in rainfall-runoff applications at the catchment and hillslope scales (Cea et al., 2022; García-Alén et al., 2022; Sanz-Ramos et al., 2021). In both cases the bed friction is discretised with a semi-implicit scheme in order to enhance the numerical stability of the solver (Cea & Vázquez-Cendón, 2012).

The suspended sediment transport equation is solved using the explicit finite volume scheme for scalar transport equations described in (Cea & Vázquez-Cendón, 2012), which ensures the conservation of the mass of sediment. The main particularity of equation (6) with respect to a typical scalar transport equation are the source terms, namely $D_{rdd,k}, D_{rdrd,k}, D_{fdd,k}, D_{fdrd,k}, D_{dep,k}$. In order to guarantee the positiveness of the suspended sediment concentration, special care must be taken with the discretisation of the deposition rate ($D_{dep,k}$), since it is the only negative source term in equation (6). For this reason, the solver implements an implicit discretisation of the deposition rate that guarantees the positivity of the suspended sediment concentration and the conservation of mass. At the same time, the rainfall and flow driven redetachment rates (D_{rdrd} and D_{fdrd}) are limited to the availability of sediment in the loose sediment layer, in order to avoid negative values of the mass of sediment in equation (15), while the detachment rates (D_{rdd} and D_{fdd}) are limited to the availability of sediment in the original soil layer.

Most of the applications of the soil erosion model imply the presence of dry regions in the computational domain. The numerical discretisation ensures the conservation of the mass of water and sediment even in the presence of wet-dry fronts. Nevertheless, for computational efficiency, a wet–dry tolerance parameter is defined, such that if the wa-

ter depth in a computational cell is lower than this tolerance the cell is considered to be dry. The numerical treatment of wet-dry fronts is described in detail in Cea et al. (2010), and follows the discretisation proposed originally by Brufau et al. (2004).

3.2 GPU implementation

The standard version of Iber was developed in Fortran following a single-threaded programming model. This makes it easier to develop and debug than programs with a parallel programming model (Sutter & Larus, 2005; Belikov et al., 2013). However, it presents strong limitations in terms of computational efficiency, since modern hardware offers most of its computational capabilities as parallel resources (Sutter, 2005; Garland et al., 2008). The single-threaded programming strongly limits the efficiency and spatial resolution of the model in applications covering large domains and/or the execution of a large number of simulations (e.g. sensitivity analysis and calibration). In order to overcome the limitations in terms of computation time, it is necessary to exploit the parallelism present in the current hardware architectures through High Performance Computing (HPC) techniques.

One cost-efficient solution quite popular in the last years is to use Graphical Processing Unit (GPU) computing. GPUs are designed with massive-parallel architectures, within the order of thousands of processing cores that can work in parallel. This provides a high amount of computational power, especially compared with consumer Central Processing Units (CPU) (Sun et al., 2019). Their characteristics make GPUs suitable not only for graphics but also for many other intensive computing applications like numerical modelling (Michalakes & Vachharajani, 2008; Grand et al., 2013; Domínguez et al., 2021), in which case they are called General Purpose Graphical Processing Units (GPGPU). GPU computing technology is available in a wide range of environments: from laptops to HPC data centers, and can be adapted to a wide range of cases of use, from prototyping to the execution of large simulations. In the last years they have been applied to many 2D-SWE codes, showing speed-ups of two orders of magnitude (García-Feal et al., 2018; Echeverribar et al., 2019; Xilin et al., 2019; Morales-Hernández et al., 2021).

In order to address the limitations in computational efficiency of the single-threaded implementation of Iber, a new object-oriented implementation of the solver was devel-

oped in C++ and Nvidia CUDA (Compute Unified Device Architecture) (NVIDIA, 2023) employing HPC techniques to take advantage of GPU computing capabilities. This new implementation, named Iber+, can achieve speed-ups of two orders of magnitude when compared with the non-parallelised version (García-Feal et al., 2018). Both implementations can be used on GNU/Linux as well as on Microsoft Windows systems, and are freely available to download from its official website (`https://www.iberaula.com`). The initial version of Iber+ only offered the parallelisation of the hydraulics and hydrology modules, implementing later on a water quality module (García-Feal et al., 2020). Following the same strategy, the new soil erosion module was parallelised on GPU.

Parallel programming, and especially GPGPU programming presents certain challenges that must be considered when developing software for these platforms. In GPUs, synchronisations between execution threads are expensive, especially global synchronisations that involve a large number of threads. This implies that certain algorithms must be rewritten to avoid or reduce the number of synchronisation operations. To deal with this, Nvidia provides libraries like CUB (CUDA Unbound) (Merrill, 2013) that offer generic high-performance parallel implementations for operations like reductions or scans. Even though some algorithms that require many synchronisations can be faster on CPU than on GPU, it should be noted that GPUs have their own high-bandwidth memory to support the massive parallelism. However, the memory transfers from the regular CPU system memory to the GPU memory is usually bottle-necked by the PCI (Peripheral Component Interconnect) bus. It is therefore advisable to minimise these memory transfers, being even preferable to perform tasks on the GPU that could be faster on the CPU to avoid costly memory transfers that reduce the global performance.

All these issues were considered in the GPU implementation of the soil erosion module in order to optimise its computational performance. The execution flow chart of the Iber+ code is shown in Figure 3. Once the input data is read and the simulation is initialised on the CPU, the data is transferred to the GPU memory and the main computation loop starts. It is the CPU that controls the main loop, being responsible for launching the GPU computations and incrementing the time counter of the simulation. In this way, for each computation time step, the memory transfers are minimised to a single variable, i.e. the current simulation time step. Only at the time steps in which it is necessary to write the results to the output files, the data is transferred back to CPU mem-

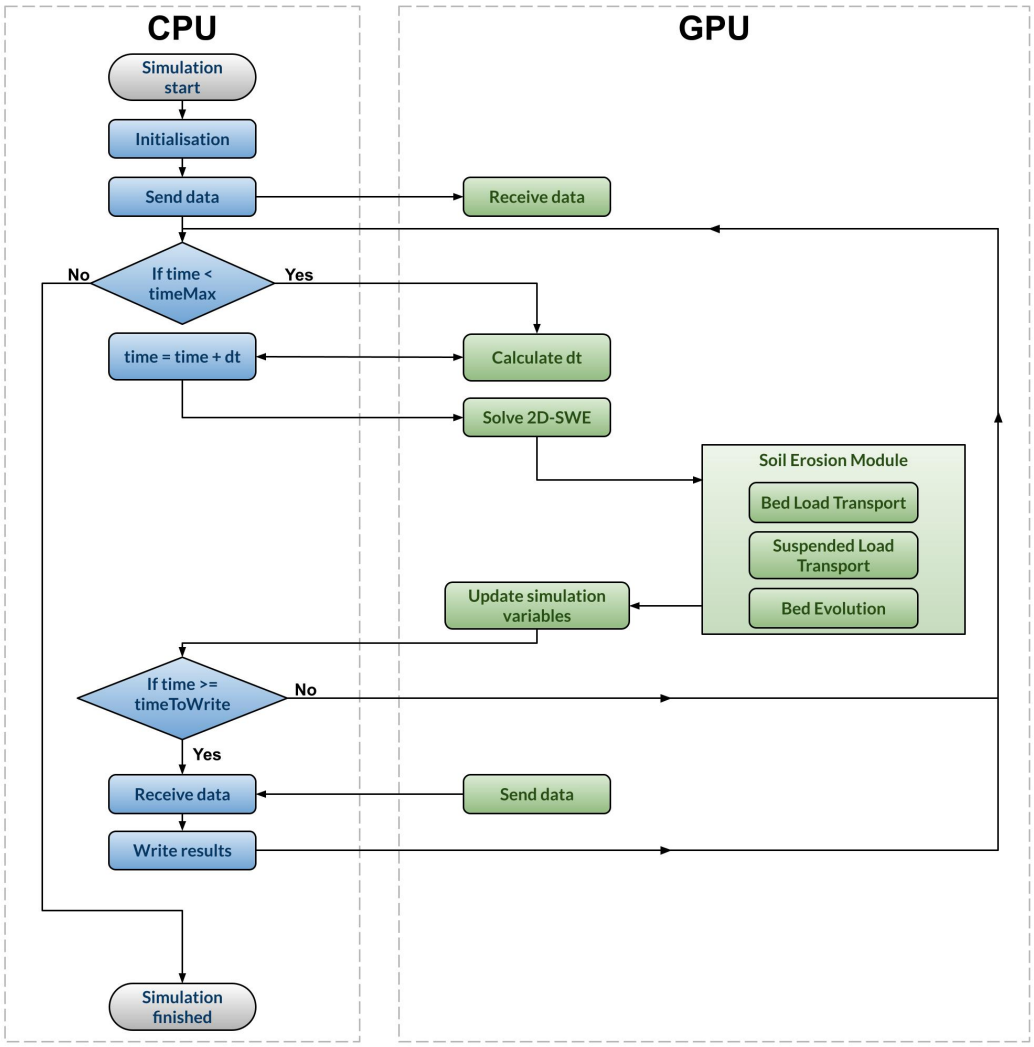

Figure 3. Flow chart of the GPU implementation

ory. The output files are written to disk by the CPU in a background thread, while the simulation continues running on the GPU.

4 MODEL APPLICATION AND VALIDATION

This section presents four test cases that cover different potential applications of the soil erosion model described in the previous sections, going from the laboratory scale to the catchment scale (Table 1).

The mathematical formulations described above require a detailed definition of several parameters and soil properties. Many of these parameters are difficult to measure,

and their calibration with field data in practical applications is complex due to the scarcity of comprehensive field data available for calibration, the uncertainty in field measurements and input data, the high non-linearity of the model equations, the interaction between input parameters, and the high spatial and temporal variability of the physical processes involved in soil erosion. All these contribute to the well-known equifinality problem in hydrological and soil erosion modelling (Beven, 2006; Vrugt et al., 2009), implying that several combinations of the input parameters can produce a similar model output. Therefore, it is complex to calibrate and run a soil erosion model including all the available processes and parameters. Instead, simplifications must be done in order to include the most relevant processes in such a way that the number of input parameters and calibration efforts are reduced (Cea et al., 2016). This task relies on the modeller and depends on the specific case study, as well as on the availability of input and calibration data. In this context, *model configuration* is understood as the selection of processes, formulations and parameterisations used in a specific case study. The number of possible model configurations is huge and the four test cases included in this section are just intended to show some relevant potential applications of the model by focusing in different soil erosion processes.

In the first test case the model is validated against the experimental results of soil erosion in a 6 m long and 2 m wide laboratory flume presented by Tromp-van Meerveld et al. (2008). Model output is compared with the observed time series of sediment flux for seven size classes, in order to asses its capability to represent size-selectivity processes at the laboratory scale. The second case presents the application of the model to a plot of 60 x 2.2 m (132 m^2) located in a hillslope with vineyards cultivated in the slope direction. Solid and liquid discharges measured at the terrain outlet during 4 rainfall events are used to calibrate and validate the model. The third case study is a headwater mountain catchment of 20 km^2 located in the French Alps, and it is used to show the sensitivity of the solid discharge computed at the basin outlet to the spatial variability of rainfall. The last test case shows the capability of the model to compute bed load transport and morphological changes at the river reach scale, using for that purpose the observed effects of the debris flood that occurred on the Ullion creek (France) during the storm Alex, in October 2020.

Table 1. Test cases used to show the performance of the soil erosion model.

Test case	Spatial scale	Area (m2)	Mesh elements	Forcing	Rainfall spatial variability	Type of transport	Sediment classes	Analysed variables	Approach
T1	Laboratory	12	120	Rainfall	No	Suspended load	7 particle sizes	Q(t), Qs(t)	Experimental validation
T2	Hillslope	120	3300	Rainfall	No	Suspended load	1	Q(t), Qs(t)	Field validation
T3	Catchment	2.00E+07	94119	Rainfall	Yes	Suspended load	4 spatial origins	Qs(t)	Sensitivity to rainfall variability
T4	River reach	1.23E+07	45314	Discharge	NA	Bed load	1	Zb(t)	Field validation

4.1 Multiclass rainfall driven erosion in a laboratory flume

Tromp-van Meerveld et al. (2008) conducted a series of rainfall driven soil erosion experiments in a 6 m long and 2 m wide rectilinear flume. The bed of the flume was made of a sediment mixture with grain sizes ranging from clay to sand. Time series of sediment concentration for seven size fractions ($<$ 0.002, 0.002-0.020, 0.020-0.050, 0.050-0.100, 0.100-0.315, 0.315-1.0 and $>$1.0 mm) were measured at the flume outlet, and will be used here to compare with the predictions of the numerical model. The proportion of these seven particle classes in the original soil (g_k) varies within 0.075 for the coarsest fraction and 0.225 for the finest ones (Table 2). Here, we used the conditions of experiment H3, in which the slope of the flume was 2.2% and a rainfall intensity of 47.5 mm/h was imposed during 2 hours. Infiltration was estimated to be 3.2 mm/h by the authors of the experiments. Rill formation was not observed during the experiments, suggesting that rainfall driven erosion was the only relevant erosion mechanism.

This experiment was reproduced numerically by Tromp-van Meerveld et al. (2008) using an analytical solution of the Hairsine-Rose erosion model that assumes steady state and spatially uniform hydraulic conditions. Several calibration alternatives were considered in their work, the main conclusion being that, in order to correctly reproduce the

sediment concentration of all classes at the flume outlet, the settling velocity of each size class had to be adjusted individually. Tromp-van Meerveld et al. (2008) give a number of possible reasons why adjusting the settling velocity is necessary, among which: 1) the formation of aggregates of clay and silt (floculation) with a larger settling velocity than the individual particles; 2) shallow water depths of the order of a few mm that prevent the largest particles from reaching their final settling velocity; 3) hindered settling due to high sediment concentrations (Baldock et al., 2004); 4) the effect of turbulence on the settling velocity (Kawanisi & Shiozaki, 2008; Pasquero et al., 2003); 5) a higher infiltration rate at the beginning of the experiment leading to a larger settling velocity for the smallest particles and; 6) errors in the measurement of the particle size distribution of the original soil. Most of these effects would tend to increase the theoretical settling velocity of the smallest fractions and to reduce the settling velocity of the largest fractions.

For modelling purposes, in this work we have discretised the rectilinear flume with 5 cm long and 2 m wide rectangular elements (in whole, 120 mesh elements). This is equivalent to a 1D mesh with a grid size of 5 cm. Since water depth data is not available to calibrate the bed roughness, the Manning coefficient was fixed to $n = 0.020$ s.m$^{-1/3}$, which is a consistent value for a flat bed with a 1 mm grain size. A critical depth boundary condition was imposed at the flume outlet and the only external forcing was a constant and uniform rainfall intensity of 47.5 mm/h during two hours. The infiltration rate was fixed to a constant value equal to the measured one, i.e. 3.2 mm/h.

Regarding the configuration of the Iber soil erosion model, the seven size classes that were measured in the experiments were considered (Table 2). Following a similar approach as in Tromp-van Meerveld et al. (2008), only suspended load and rainfall driven erosion were considered in the model, and the rainfall detachment and redetachment erodibility coefficients were assumed to be constant for the seven size classes (i.e. $\alpha_{d,k} = \alpha_d$ and $\alpha_{rd,k} = \alpha_{rd}$ for all particle classes k). Due to the small water depths in the flume (of the order of 1-2 mm), it was assumed that rainfall damping was negligible and thus, the rainfall damping factor was fixed to one ($f_d = 1$). On the other hand, the critical mass in the eroded layer ($M_{s,cr}$) was manually calibrated. This parameter has a significant influence in the results, since it is used to compute the shield factor (ε) in equation (8), and it controls the initial concentration peak in the sedigraphs of the smallest size classes.

Table 2. Add caption

Class (k)	Size (mm)	g_k	D_k (mm)	$w_{s,k}$ (mm/s)	$w_{s,eff}$ (mm/s)	correction factor	correction factor in (Tromp-van Meerveld et al., 2008)
1	< 0.002	0.225	0.001	0.001	0.003	4.0	3.5
2	0.002 - 0.020	0.225	0.011	0.11	0.54	5.2	4.5
3	0.020 - 0.050	0.125	0.035	1.07	25.07	23.5	9.0
4	0.050 - 0.100	0.125	0.075	4.90	58.05	11.8	8.5
5	0.100 - 0.315	0.125	0.208	26.48	70.77	2.7	15.0
6	0.315 - 1.0	0.100	0.658	87.46	70.77	0.8	0.7
7	> 1.0	0.075	1.0	137.74	70.77	0.5	0.4

The values of the three previous parameters were manually calibrated to $\alpha_d = 100$ g/m^2/mm, $\alpha_{rd} = 10000$ g/m^2/mm and $M_{s,cr} = 0.13$ kg/m^2. In addition, for the reasons given in (Tromp-van Meerveld et al., 2008) and mentioned above, it was necessary to adjust the settling velocity of each sediment class in order to correctly reproduce the observed time series of suspended concentration for the seven classes (Figure 4). The adjusted settling velocities, as well as the correction factors defined as the ratio between the effective and theoretical settling velocity (the latter one computed with the formula of van Rijn (van Rijn, 1984)), are shown in Table 2. The correction factors are larger than one for the five smallest sediment classes, and smaller than one for the two largest sizes. Notice also that the effective settling velocities for the three largest sizes is the same. These results are consistent with those of Tromp-van Meerveld et al. (2008), although the correction factors are slightly different, as shown in Table 2.

With the previous parameterization the model is able to reproduce the observed sedigraphs with Mean Absolute Errors (MAE) ranging from 5% to 20% of the peak concentration for each sediment class (Figure 4). The global trend of the concentration time series is properly captured for the seven classes, with an accurate estimation of the peak concentration for the smallest fractions. The MAE for the total concentration time series is 1.22 g/l, for a maximum concentration of 33 g/l (i.e. 4 % relative error).

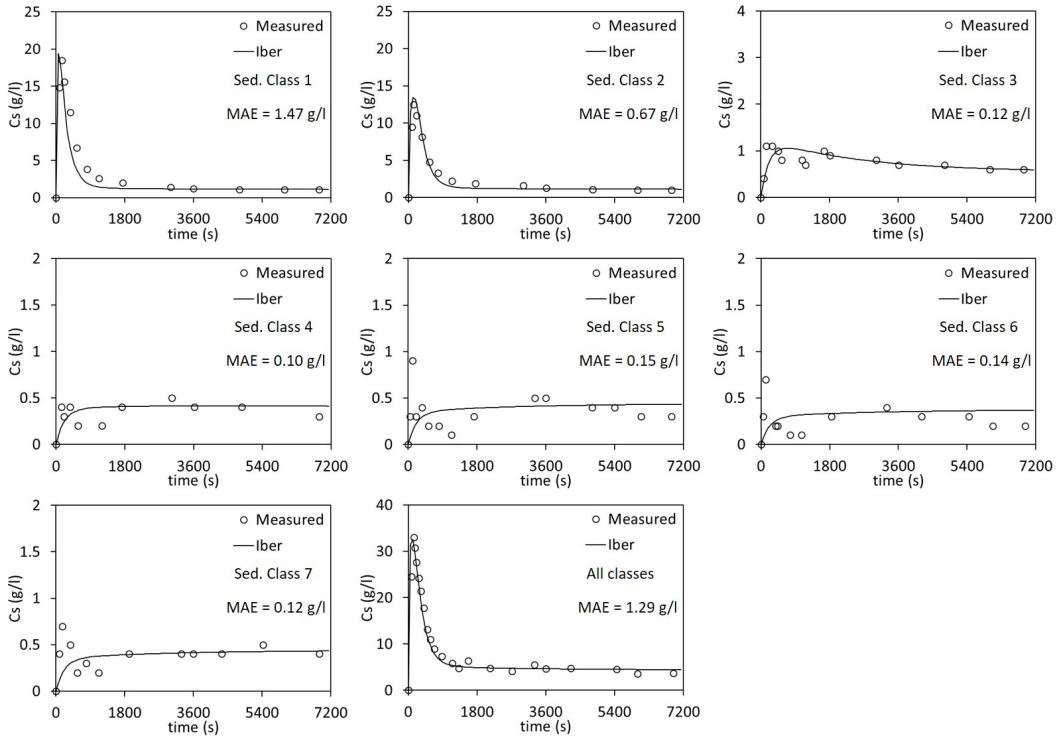

Figure 4. Computed and measured (Tromp-van Meerveld et al., 2008) time series of sediment concentration at the laboratory flume outlet.

4.2 Rainfall and runoff driven erosion at the hillslope scale

In the second test case the model was applied to a Mediterranean hillslope vineyard of 130 m^2 located in Ardèche (south eastern France), which is part of the Olivier de Serres site of the Cévennes – Vivarais Mediterranean Hydrometeorological Observatory (OHMCV) (Boudevillain et al., 2011). The hillslope is 60 m long and 2.2 m wide. Its topography was measured at 15 cross sections and 6 points per cross section, with an uncertainty of 1 cm in the three dimensions. The average longitudinal slope is around 15%, and there is a natural rill that conveys all the surface runoff to the foot of the hillslope, with no runoff losses through the lateral sides (Figure 5). The soil is calcareous and covered by sparse vegetation, with an approximate composition of 34% clay, 41% silt and 25% sand.

The soil erosion data monitored during the four storm events included in Table 3 were used to calibrate and validate the model. These data sets and the DEM of the vineyard are described in detail and can be downloaded from Nord et al. (2017). Rainfall was

446 measured with a raingauge located at the downstream end of the hillslope. The outlet
447 discharge was measured continuously with an H-flume located at the downstream out-
448 let. The concentration of sediment at the outlet was estimated from water samples taken
449 within the H-flume using an automatic sampler. Samples were taken only when prede-
450 fined thresholds of water discharge or discharge variations were exceeded. Thus, depend-
451 ing on the storm event, between 11 and 21 sediment concentration measurements were
452 done. Specific details about the instrumentation and experimental procedure can be found
453 in Grangeon (2012) and in Nord et al. (2017).

454 The maximum 1-minute rainfall intensity in the storm events analysed varies within
455 24 and 92 mm/h, while the outlet discharge varies between 0.30 and 1.73 l/s, and the
456 maximum suspended sediment concentration between 0.18 and 1.42 g/l.

457 In the numerical model the hillslope was discretised with a structured mesh and
458 a uniform cell size of 0.20 m (3,300 mesh elements). Given the small size of the hillslope,
459 all the numerical parameters and input data were assumed to be uniform in space. Con-
460 sidering that the average slope in the longitudinal direction is about 15%, and the con-
461 figuration of the H-flume located at the hillslope outlet, a critical depth condition was
462 imposed at the downstream boundary. The inlet discharge at the upstream boundary
463 was zero, and the only external forcing was the rainfall intensity measured by the rain-
464 gauge, which was imposed in the model with a rainfall depth resolution of 0.2 mm. As
465 mentioned above, the surface runoff is confined in the transverse direction by the topog-
466 raphy, preventing any water or sediment fluxes through the lateral boundaries.

467 The bed roughness was characterised with the Manning coefficient, and its value
468 was calibrated manually for each event, since the macro-roughness of the hillslope (in-
469 cluding vegetation) varies from one season to another, depending on the tillage. Rain-
470 fall losses were estimated with a simple model that consists on an initial abstraction (I_a)
471 and a constant potential infiltration rate (k_s). The initial abstraction is subtracted from
472 the input rainfall, while the infiltration rate is subtracted at each computational time
473 step from the surface runoff depth at each mesh element, as long as the local water depth
474 is enough to satisfy the potential infiltration rate. Regarding soil erosion, a relatively sim-
475 ple model configuration was considered, with a single loose sediment layer of infinite thick-
476 ness (i.e. unlimited availability) and only two erodibility parameters that control the rain-
477 fall and runoff driven redetachment (F and α_{rd} respectively). Therefore, five input pa-

rameters were used to calibrate the model, namely I_a, k_s, n, F and α_{rd}. From these, the three parameters that control the transfer of water (I_a, k_s, n) were allowed to vary from one event to another in order to reproduce as accurately as possible the observed outlet hydrographs, while the two parameters that model the transfer of sediment (F and α_{rd}) were calibrated for the storm event R1 and maintained constant for the other three validation events (Table 4).

The computed and observed hydrographs and sedigraphs at the hillslope outlet are shown in Figure 6. The agreement between the numerical and observed hydrographs is very good in the four events, suggesting that the surface runoff is correctly reproduced by the model and that the hydraulic variables involved in the runoff-driven erosion are properly predicted. Regarding the sedigraphs, using the same erodibility parameters in the four events, the model is able to reproduce the order of magnitude and the time variability of the sediment fluxes, with Nash–Sutcliffe Efficiency (NSE) values ranging from 0.66 to 0.91 and Mean Absolute Errors (MAE) that vary between 4% and 13% of the maximum observed solid discharge for each event (Table 4).

Table 3. Characteristics of the four storm events in the hillslope vineyard (test case 2).

Event	Start	Max. 1 min rain intensity (mm/h)	Rain depth (mm)	Runoff duration (h)	Runoff depth (mm)	Qmax (l/s)	Cs,max (g/l)
R1	09/11/2012 22:00	24	65	10	12	0.30	0.18
R2	04/11/2011 12:00	79	129	3.9	17	0.98	1.32
R3	18/05/2013 08:00	80	46	5	29	1.73	0.76
R5	20/10/2013 06:00	92	64	2.6	29	1.35	1.42

4.3 Spatial variability of rainfall driven erosion at the catchment scale

The aim of this test case is to show the effect of the spatial variability of rainfall at the catchment scale on the modelled water and sediment fluxes at the basin outlet. The soil erosion model was applied to the Galabre basin, a 20 km^2 meso-scale headwater catchment located in the French Alps that is part of the Draix-Bléone Observatory.

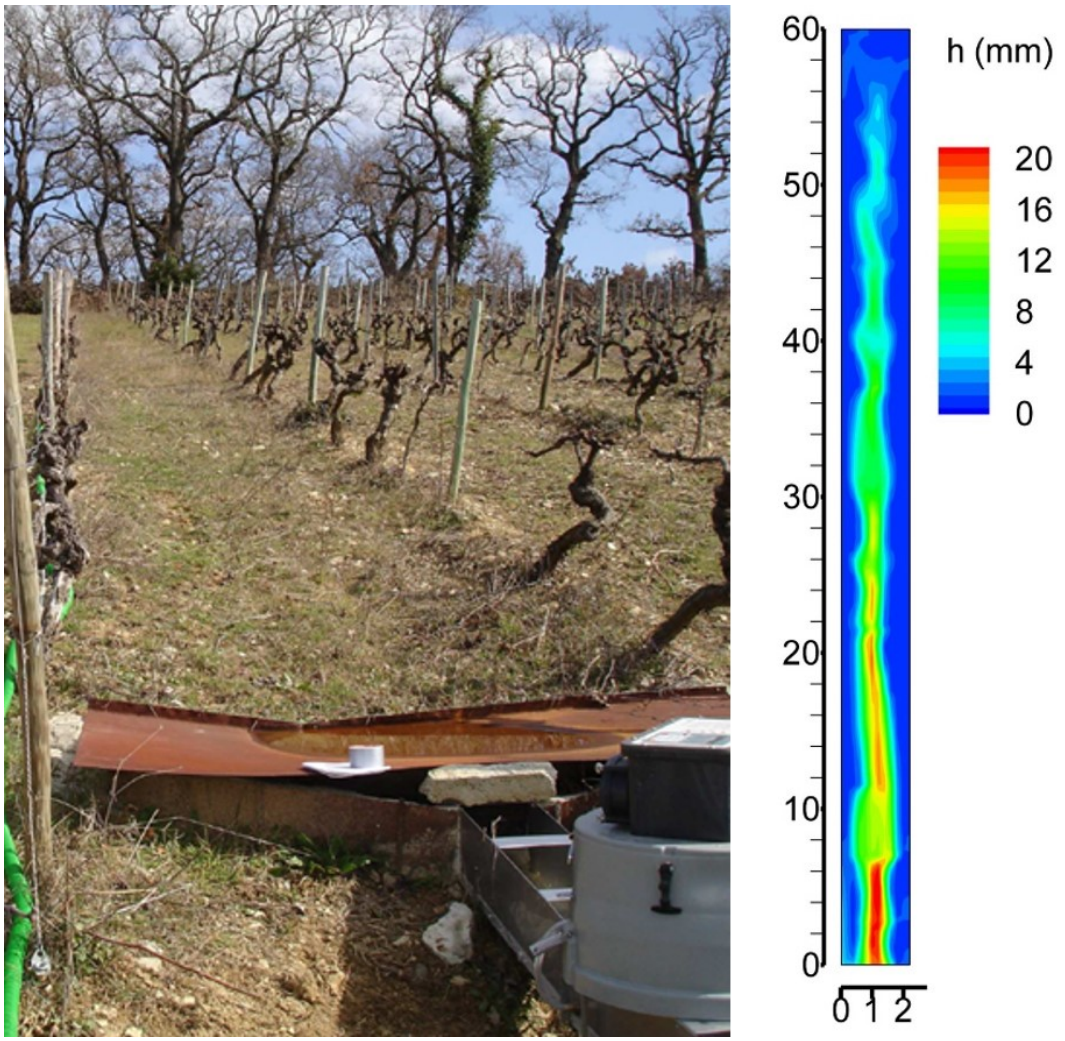

Figure 5. Hillslope vineyard (left) and typical water depth pattern during a storm event (right) in test case 2.

Table 4. Model parameters and performance results for the four storm events analysed in the hillslope vineyard (test case 2). The performance results refer to the agreement between observed and computed sedigraphs at the hillslope outlet.

Event	n (s/m$^{1/3}$)	I_a (mm)	k_s (mm/h)	α_{rd} (g/m^2/mm)	F (x10^{-3})	$MAE/Q_{s,max}$	NSE
R1	0.6	36	1.8	20	0.001	0.10	0.74
R2	0.3	11	1.3	20	0.001	0.04	0.91
R3	0.2	11	0.0	20	0.001	0.09	0.66
R5	0.8	32	0.9	20	0.001	0.13	0.70

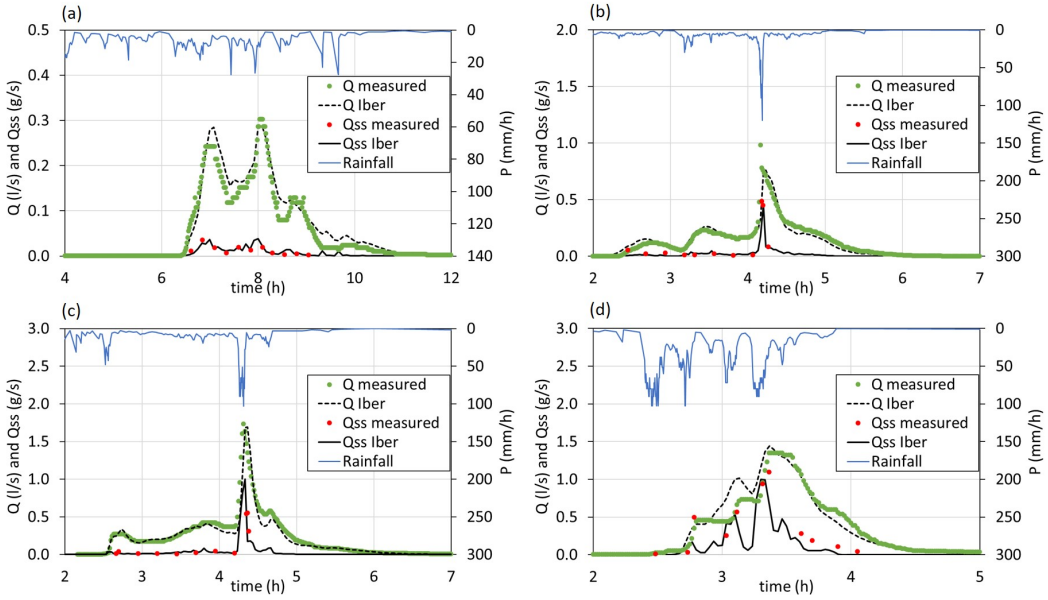

Figure 6. Numerical and observed outlet hydrographs and sedigraphs for the four rainfall events analysed in the hillslope vineyard (test case T2). Events: (a) R1, (b) R2, (c) R3 and (d) R4.

Liquid and solid discharges are continuously monitored at the catchment outlet (Legout et al., 2021).

The main types of lithologies in the catchment are limestones, marls, molasses and quaternary deposits. Around 10% of the catchment surface is covered by dispersed badlands that constitute the main source of sediment at the basin outlet (Esteves et al., 2019; Poulenard et al., 2012; Legout et al., 2013). The rest of the land is permanently covered by forests and bushes, contributing to a much less extent to the sediment yield.

The numerical discretisation of the basin was done with an unstructured mesh of triangular elements, using different element sizes in the hillslopes, badlands and river network. This way of building the mesh has the advantage of using a higher spatial resolution in the regions where the water and sediment fluxes concentrate, i.e. in the river streams and in the badlands. Similar discretisation schemes for solving the 2D-SWE in hydrological applications have been used for instance in Cea et al. (2022); Costabile and Costanzo (2021); Ferraro et al. (2020). The main river network was defined from a DTM of the catchment with a spatial resolution of 1 m, assuming a Contributing Drainage Area (CDA) of 500 ha to define the perennial water streams, and a CDA of 15 ha to define

514 the intermittent streams composed of small tributaries. The river network obtained us-
515 ing these thresholds is shown in Figure 7, and it is coherent with *in situ* observations (Uber
516 et al., 2021). The computational mesh was built considering this stream network as well
517 as the location of the badlands shown in Figure 7. On the hillslopes, a mesh size of 100
518 m was used in order to avoid an excessively high number of elements. On the badlands,
519 where the sediment fluxes originate, a mesh size of 20 m was used. The mesh size was
520 refined to 5 m inside a buffer layer along the river network. This buffer layer was 5 m
521 and 10 m wide on both sides of the river network, for the intermittent and the peren-
522 nial streams respectively. Such widths are consistent with the approximate width of these
523 streams in the catchment. With this discretisation scheme, the number of mesh elements
524 was around 94000. Following (Uber et al., 2021), the Manning bed roughness coefficient
525 was set to 0.05 in the river network and to 0.80 in the hillslopes.

526 Soil erosion was modelled for a rainfall event recorded on 23/06/2010, prescribing
527 the effective rainfall intensity in two different ways: 1) as spatially distributed rainfall
528 fields defined from raster files with spatial and temporal resolutions of 1 km and 15 min-
529 utes respectively and 2) as spatially uniform rainfall fields defined as the spatial aver-
530 age of the rainfall fields over the entire catchment, with a time resolution of 15 minutes.
531 Both rainfall products are equivalent in terms of the spatial average of rainfall intensity
532 at each time step. The only difference between both simulations was the spatial variabil-
533 ity of rainfall. The spatial distribution of rainfall depth for the entire event over the whole
534 catchment is shown in Figure 7.

535 For modelling purposes, only the rainfall driven erosion was considered with a sin-
536 gle loose sediment layer of infinite thickness (i.e. unlimited availability), and the produc-
537 tion of sediment was limited to the badlands. Four different sediment types were defined
538 according to the four lithologies in which the badlands are developed, i.e. limestones, marls,
539 molasses and quaternary deposits (Figure 7). The rainfall erodibility coefficient was as-
540 sumed to be the same for all the badlands in order to focus the analysis on the effect of
541 the spatial variability of rainfall. Its value ($\alpha_{rd} = 7.4 \mathrm{g/m^2/mm}$) was taken from Uber
542 et al. (2021), where its average value was estimated from the interannual observed rain-
543 fall depth and suspended sediment yield at the catchment outlet.

544 Figure 8 shows the relevance of considering the spatial variability of rainfall when
545 modelling soil erosion in this meso scale catchment. The hydrographs and sedigraphs com-

puted differ significantly between the two scenario, not only in their peak values, but also in the total sediment yield (Table 5). When assuming a spatially uniform rainfall field the peak discharge diminishes considerably compared to the spatially variable case (from 104.7 to 62.3 m^3/s), since in the former case the rainfall intensity is homogeneously distributed over the entire catchment, instead of being concentrated around the basin outlet, as it is when its spatial variability is considered (Figure 7). The effect is similar when looking at the fluxes of marls and limestones, which originate from badlands that are more or less distributed all over the catchment. For these two sediment types the peak fluxes are significantly higher when considering the rainfall variability (Table 5). On the contrary, molasses and quaternary deposits are mainly located in the upper part of the catchment and they are eroded at a much lower rate when the spatial variability of rainfall is considered in the model, since the observed rainfall depth was very low in this part of the catchment. For these two sediment types the peak fluxes are much smaller when considering the spatially variable rainfall field.

Table 5. Water and sediment fluxes computed in the Galabre catchment with spatially uniform and variable rainfall fields.

	Peak flux (m^3/s for water and ton/s for solid)				
Rainfall input	Water	Limestones	Marls	Molasses	Quaternary
Uniform	62.3	4.0	25.4	5.7	6.8
Rasters	104.7	8.7	35.6	0.5	2.7
	Total mass flux (m^3 for water and ton for solid)				
Rainfall input	Water	Limestones	Marls	Molasses	Quaternary
Uniform	430596	39.3	145.9	21.4	47.7
Rasters	449214	36.5	92.5	3.1	8.2

4.4 Massive bed load deposition during a debris-flood event

The aim of this case study is to demonstrate the capability of the model to correctly reproduce in-channel processes, as very active bed load transport. An un-published analysis of the Ullion creek debris-flood that occurred during the Alex Storm (2 - 3 Oct.

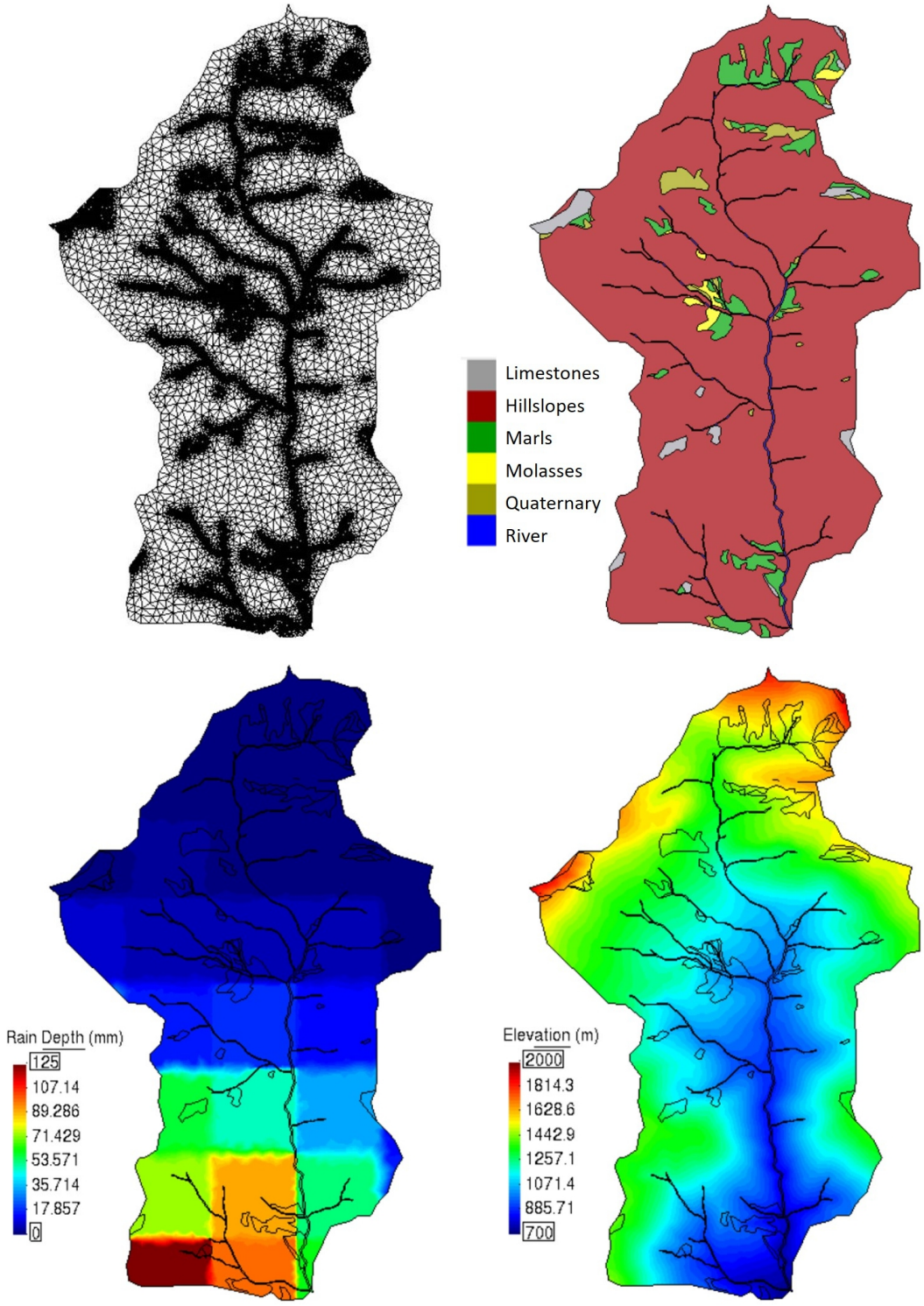

Figure 7. Galabre catchment. Computational mesh (upper-left), spatial distribution of lithologies (upper-right), spatial distribution of rainfall depth for the 23/06/2010 storm (lower-left) and topography (lower-right).

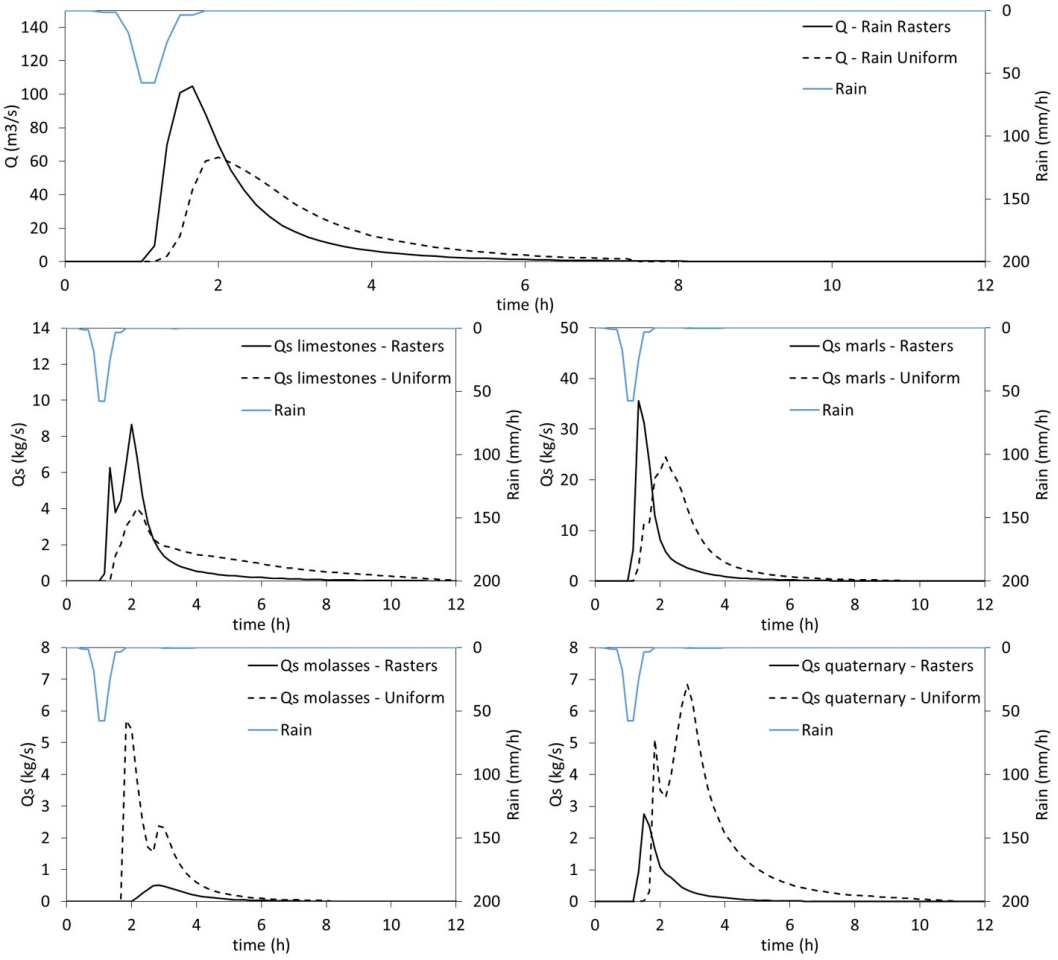

Figure 8. Hydrographs and sedigraphs computed in the Galabre catchment using spatially uniform and variable rainfall fields.

2020) exemplifies that the present soil erosion module can also be used to focus solely on river channels (Piton & Rodier, 2022).

The Ullion Creek is a tributary of the Tinée River in the south east of France. Its 12 km^2 catchment is very steep, ranging from 2087 m.a.s.l. to 356 m.a.s.l. at the confluence with the Tinée (Figure 9a). Only the last 1.5 km of this 7.7 km long creek was modelled in this study. The creek channel is confined between steep hillslopes until the confluence (Figure 9b), and has a very uniform longitudinal slope of 11.0% along the modelled reach (Figure 10). The Tinée River has conversely a catchment of about 600 km^2 at the confluence. Its river bed shows evidences of regular bedload transport. It has an average longitudinal slope of about 1.1%, and it flows into a valley with an alluvial floodplain located on the right bank (Figure 9c). Two roads follow the Tinée River axis near the study site, a main road on the right bank in front of the creek and an old road, usually closed, passing the creek on an old bridge (Figure 9d).

On the 2^{nd} and 3^{rd} October 2020, the Alex Storm hit the region triggering extreme rainfalls and catastrophic floods with astonishingly high sediment transport, erosion and damages to roads, infrastructures and buildings (Carrega & Michelot, 2021). The rainfall estimated from the combination of weather radar and rain gauges was higher than 500 mm on the Ullion Creek catchment within less than 24 h (Payrastre et al., 2022). A large landslide occurred in a former diffuse gullying area and fed suddenly the creek with an unlimited amount of sediment. The sediment was transported mainly as bed load, at least in the downstream part of the basin according to videos taken by local dwellers. A massive deposition occurred in the creek bed, elevating the bed level by about 7 m on average. An alluvial fan that was formed at the confluence dammed and diverted the main river to the opposite bank, thus resulting in the erosion of about 300 m of the main road (compare Figures 9d and 9f with Figures 9e and 9g). This case study is well documented as a debris-flood event, i.e. a very intense flood carrying massive amount of bed load material and involving large erosion and / or deposition (Church & Jakob, 2020).

Two DTM where obtained from LiDAR data, the first dating from 2018 (LiDAR2018@MNCA) and the second dating from two days after the event (LiDAR2020@IGN). A total volume of bed material deposit of about 330,000 m^3 was estimated from the difference between both DTM within the extend of the alluvial fan deposit and of the 1.5 km terminal reach of the creek.

The *post*-event LiDAR is available only on the terminal reach of the creek, so the analysis was focused only on this area. The event hydrographs entering the analysed Ullion creek and Tinée River reaches were reconstructed from the distributed rainfall data, using the Curve Number (CN) method with an hypotheses of flow velocities of 0.2 m/s on hillslopes and of 5 m/s in channels (personal communication with Pierre Brigode). A value of CN = 60 was taken according to field evidences and back analysis of flood marks performed by Payrastre et al. (2022). The resulting hydrograph for the Ullion catchment lasts about 23 hr, has a peak discharge of 86 m^3/s at 15:00 and a cumulated volume of 2.5 Mm^3. The ratio between the deposited bedload volume and the hydrograph volume is about 0.16, implying a very high concentration for bed load, but not uncommon during debris floods (Church & Jakob, 2020). For the Tinée, the peak discharge is 905 m^3/s and the volume 31.5 Mm^3.

As a first approximation, we assumed clear water flow at the inlet boundaries until the material coming from the landslide reached the model boundary. We then then computed the bed load discharge using the Meyer-Peter and Müeller (MPM) equation. The time at which the bedload transport wave reached the model boundary is estimated to be 15:00 $\pm$ 1:00 according to a sensitivity analysis and comparison to field observations from the local firefighters (Piton & Rodier, 2022). Grain size samples were measured *a posteriori* with $D_{50} = 23$ mm in the main body of the deposit. The Manning coefficient of the model was fixed at 0.070 $s.m^{-1/3}$ assuming a near-critical Froude number, as measured on debris-flood experiments (Piton & Recking, 2019), while in the Tinée a value of 0.045 $s.m^{-1/3}$ provided reasonable results. Tests performed with 0.04 $s.m^{-1/3}$ led to too much deposit in the channel while tests performed with 0.05 $s.m^{-1/3}$ resulted in not enough deposition. A triangular unstructured mesh was used to discretise the spatial domain, with elements of 3 m in the Ullion creek and of 5 m in the Tinée. The total number of elements of the computational mesh was around 45,000. According to our field observations, the bed channel was considered non erodible in the Ullion Creek. Conversely a 6 m-deep erodible layer was set at the confluence and 2 m-deep further upstream and downstream. These depths were selected higher than the maximum erosion measured between the two LiDAR surveys.

It is worth stressing that 2D numerical modelling including sediment transport is so far considered not mature enough to be used in studies of massive bed load transport in steep creeks, e.g. to assess debris-flood hazards (Jakob et al., 2022). In this case study,

despite using the most commonly used bed load transport equation in gravel bed rivers, namely MPM, and common values of Manning coefficients, the model provided very satisfactory results. The slope and spatial distribution of the deposit are similar to the observations (Figure 10), being slightly lower than observed in the final reach. Landforms as channels, terraces and even the alluvial fan appear in the model in a very similar fashion than in the field. In the line of the longitudinal profile being slightly lower than observed, the alluvial fan is slightly more extended toward the downstream direction than actually observed (Figures 9g & 9i). The extension of the bank erosion that destroyed the road is also reasonably captured by the model. Note that since the LiDAR data were taken while the water level was still relatively high in the Tinée River (see the flooded area represented as a hatched area in Fig. 9e), the reference erosion and deposition contour lines in Figure 9g should not be analysed in this area, the *post*-event data being the free surface level and not the actual terrain level.

Further investigations must be performed to fully understand the dynamics of this case study, which includes massive deposition and erosion at fan and confluences between steep creeks and mountain valley rivers, during an extreme flood event. The results of this test case show that the soil erosion module presented here can be used for that purpose.

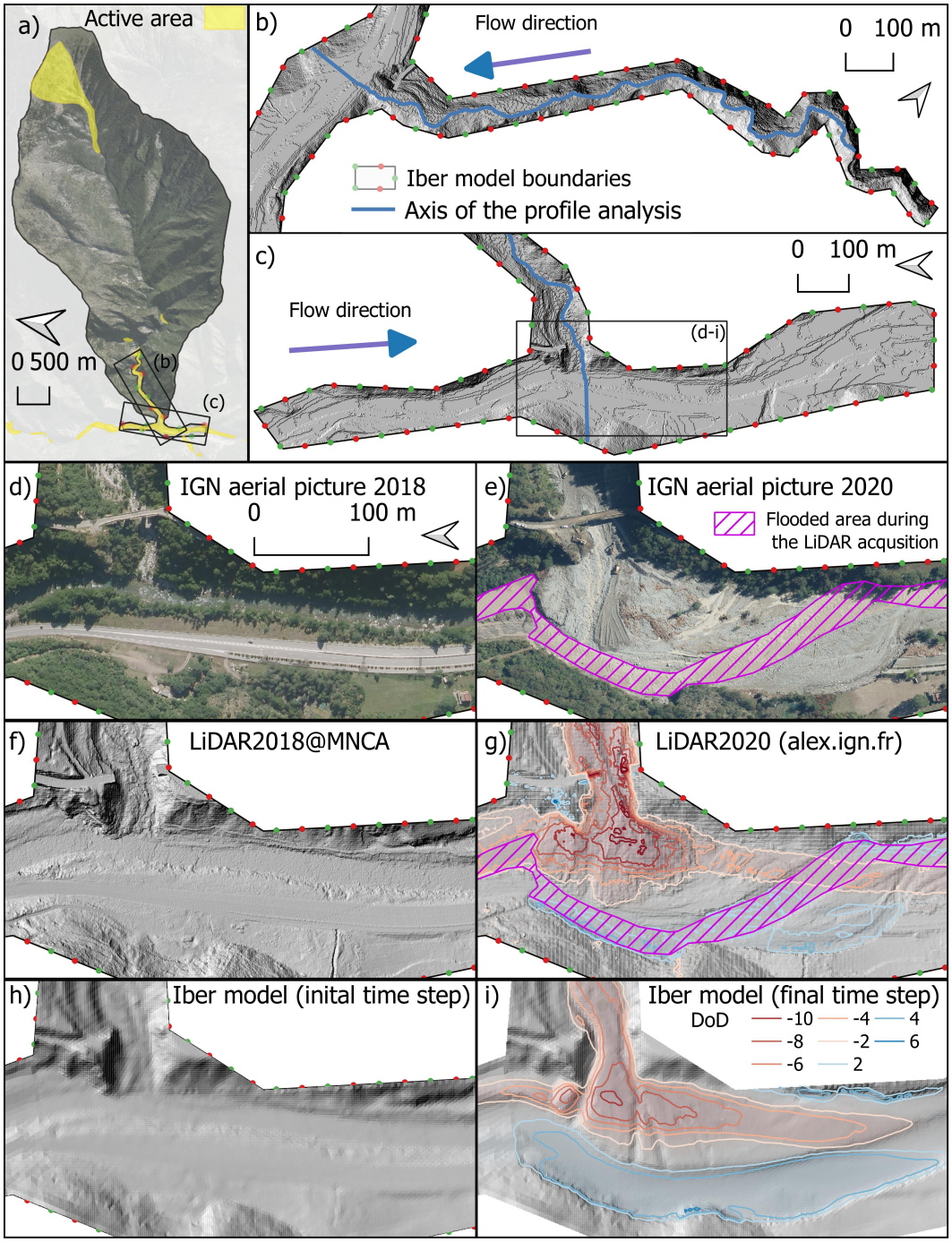

Figure 9. Ullion catchment case study: a) general view including the landsliding area in the headwaters and the deposition zone near the confluence; b) zoom on the extension of the Iber model on the Ullion Creek branch; c) zoom on the extension of the Iber model on the Tinée River branch; aerial pictures of IGN d) before and e) after the event including the hatched area where flow was still high during the LiDAR acquisition and thus the elevation reported is that of the free surface and not of the terrain; DEM digital elevation model f) before and g) after the event including coloured contour lines of the DoD (difference between initial and final DEMs); and Iber model bed elevation h) before and i) after the event including coloured contour lines of the DoD.

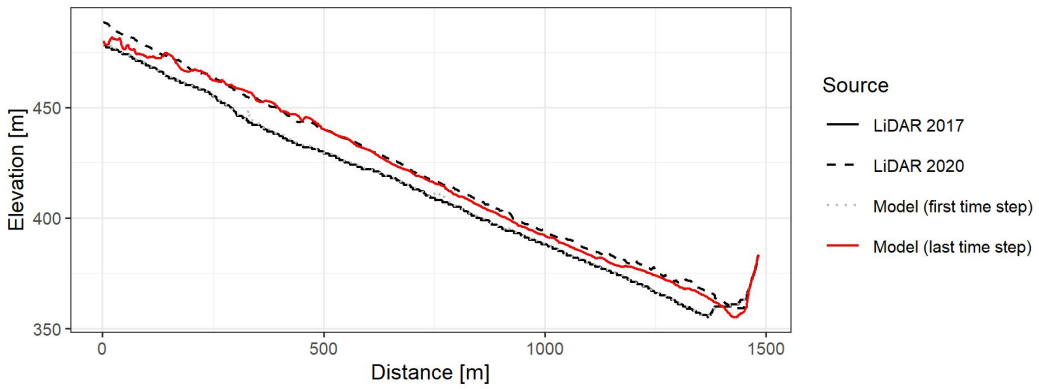

Figure 10. Longitudinal profile along the axis of the Ullion creek (blue line on Figures 9b-c) with observed and model bed states

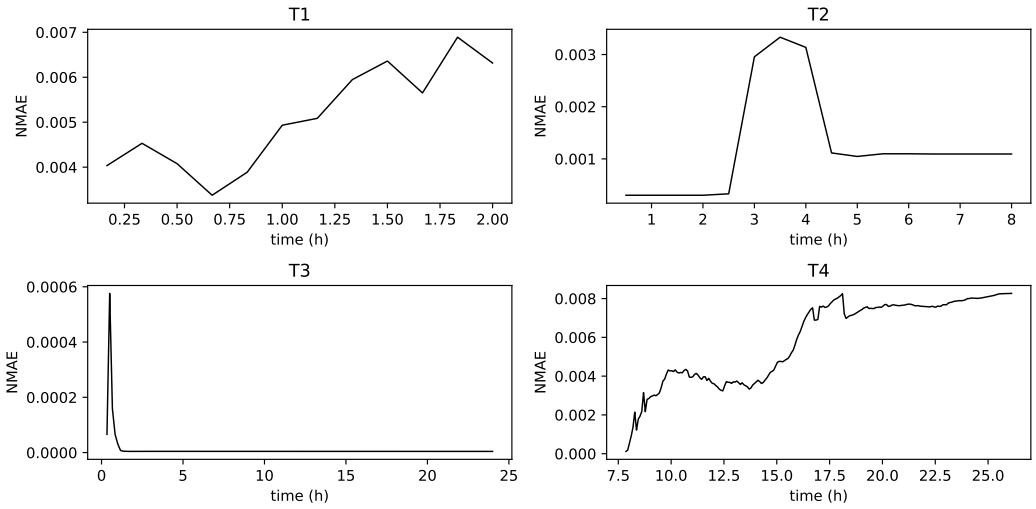

Figure 11. Normalised mean absolute error evolution of the two proposed implementations for the four proposed test cases.

5 COMPUTATIONAL EFFICIENCY

As described in section 3.2 two implementations of the soil erosion model were developed. The main one was developed to run on CPUs in a single thread, meanwhile the GPU-enhanced implementation was developed to take advantage of the parallelism present in general purpose graphic cards. Both implementations were compared in terms of accuracy and computational efficiency using the four test cases proposed in the previous section. In test case T2, only the storm event R3 was chosen from the four events analysed, due its higher computational burden, while in test case T3 the spatially variable rainfall scenario was used.

In order to quantify the difference between the two solvers solutions, the normalised mean absolute error (NMAE) was calculated:

$$MAE = \frac{\sum_{i=1}^{N} |y_i - \hat{y}_i|}{N} \qquad NMAE = \frac{MAE}{|y_{max} - y_{min}|} \tag{19}$$

where N is the number of elements of the computational mesh, y_i are the values given by Iber, $\hat{y}_i$ are the values obtained from Iber+, y_{max} and y_{min} are the maximum a minimum values of the Iber simulation for a given time-step respectively. Figure 11, shows the evolution of the NMAE for each of the proposed test simulations, keeping values below 0.0085 in all cases.

Table 6. Hardware configurations employed for the performance measurements.

Configuration	Solver	CPU	GPU		
			Model	Throughput	TDP
CPU Server	Iber	Intel Xeon Gold 6130	-	-	-
GPU Server	Iber+	Intel Xeon Gold 5218R	Nvidia V100	14.9 TFLOPS	300W
Desktop computer	Iber+	AMD Ryzen 7 2700X	Nvidia RTX 3080 ti	28.6 TFLOPS	400W
Laptop computer	Iber+	Intel Core i7-11375H	Nvidia RTX 3060	10.7 TFLOPS	115W

Several hardware configurations were used to compare both implementations (Table 6). The Iber package supports different hardware and software platforms. It can be run on Microsoft Windows and GNU/Linux operating systems, in systems that range from servers to laptops using CPU and GPU computing. In the first configuration (CPU Server), the standard non-parallelized implementation of the model was run on a server with a CPU Intel Xeon Gold 6130. This will be considered as the baseline for performance comparison. Next, the GPU parallelized version was run in three different hardware configurations. First, a GPU computing server with a GPU Nvidia V100, a datacenter oriented graphics card released in 2017 with 5120 CUDA cores that offer nearly 15 TFLOPS (10^{12} floating point operations per second) of theoretical peak throughput. Second, a standard desktop computer with a Nvidia RTX 3080 ti. This is a high-end consumer-grade graphics card released in 2021 with 10240 CUDA cores that offers over 28 TFLOPS of computing power. Lastly, the model was also run in a laptop computer featuring an Nvidia RTX 3060, a mid-tier graphics card released in 2021 with 3584 CUDA cores and a reduced TDP (thermal design power) for mobile hardware. This limits its performance to nearly 11 TFLOPS. It should be considered that the performance of the GPUs mentioned above are based on peak values given by the manufacturer, and must be taken only as a rough indicator of their actual performance, which depends on many factors as the thermals, the configuration made by the assembler, or the software. The server configurations (CPU and GPU Server in Table 6) were run on the GRICAD (Grenoble Alpe Research - Scientific Computing and Data Infrastructure) facilities and run on Debian GNU/Linux version 11 OS. The desktop computer configuration was run on Archlinux OS meanwhile the laptop computer was run on Windows 11 OS.

Table 7. Performance measurements obtained for the different test cases and hardware configurations.

	CPU Server			GPU Server			Desktop Computer			Laptop Computer		
Test case	Time (s)	Speedup	MCells/s	Time (s)	Speedup	MCells/s	Time (s)	Speedup	MCells/s	Time (s)	Speedup	MCells/s
T1	35	1	0,18	29	1.21	0.22	24	1.46	0.27	92	0.38	0.07
T2	155	1	1.37	9	17.22	23.29	8	19.38	26.20	28	5.54	7.49
T3	34271	1	0.56	283	121.1	67.24	195	175.75	97.58	542	63.23	35.10
T4	31646	1	1.82	451	70.17	129.11	406	77.95	141.68	828	38.22	69.59

Table 7 shows the run-time for the different test cases and hardware configurations. Three performance metrics are evaluated for each hardware configuration: a) the time needed to complete the main loop of the simulation (this excludes the initialisation time of the simulation), b) the speedup compared with the non-parallelised configuration and c) the throughput of the model expressed in millions of mesh elements processed per second that is computed as follows:

$$Throughput = \frac{n_{cells} \cdot n_{steps}}{t_{simulation}} \cdot 10^{-6} \tag{20}$$

where n_{cells} is the number of cells of the computational mesh, n_{steps} is the number of computational steps needed to complete the simulation and $t_{simulation}$ is the run-time in seconds of the main loop of the simulation.

The first test case (T1), is expected to be the worst scenario for the GPU parallelized implementation. This case uses a computational mesh of just 120 elements, meaning that the level of parallelism present in this problem is much lower than in the other test cases. Therefore, in this case the parallelized implementation is not capable of exploiting in an effective way the parallel computing resources available. The GPUs used have a thousands of parallel computing units (or CUDA cores), but each single core is less powerful than a single CPU core. This implies that processing 120 elements in parallel in a GPU will not saturate its computing capabilities, leaving many of the resources unused. Therefore, in this case, the high computational capacity of the GPU cannot overcome the overhead of using it (e.g. GPU memory transfers, expensive synchronizations, etc.). As shown in Table 7, the T1 case ran in 38 seconds on the CPU server. The runs

on the GPU server and on the desktop computer were just marginally faster (29 and 24 seconds respectively), while running on the laptop was significantly slower (92 seconds).

The T2 test case has a larger computational mesh of 3,300 elements, which is still lower than the number of cores of the GPUs. However, it is large enough to see some significant performance gains compared with the CPU solver. While the CPU version took 161 seconds to finish the simulation, the GPU server and the desktop computer were able to perform the simulation over 17 and 19 times faster respectively, while the laptop ran 5 times faster. The performance in terms of the number of processed cells per second increased in all configurations compared to T1. In the CPU version, this value is over 7 times higher. This is mainly due to the higher presence of dry elements (that are much faster to process) in test case T2. Also, this case uses just a single class of soil particles, meanwhile T1 uses seven different classes that must be processed independently. It is noteworthy that in the case of the GPU configurations the number of cells processed per second was increased over 100 times in comparison with T1, denoting that this case is more effective exploiting the parallel computing resources available on the GPU.

The test case T3 has the largest computational mesh from all the proposed cases, with 94,119 elements. This number of elements is expected to be large enough to show the full potential of the GPU implementation. This case took more than ten hours to be processed by the CPU configuration. However, it took less than five minutes on the GPU server, achieving a speedup of 121. It was even faster in the desktop computer, with a speed-up of 176 relative to the CPU. The laptop configuration achieved a speed-up of 63, showing the capabilities of the GPU computing even on modest devices. In terms of throughput, the number of cells processed per second was reduced in the CPU compared with T2, lowering from 1.37 MCells/s to 0.56, mostly due to the increase of soil particle classes (from 1 to 4) and the lower presence of dry elements in T3. However, in the case of the GPU configurations, the number of cells processed per second increased significantly due to the bigger size of the mesh. Hence, the higher number of elements enabled a better exploitation of the parallel resources.

The last test case (T4) has a computational mesh of 45,314 elements. This is less than T3, hence a lower speedup was expected due to lower occupancy of the GPU. This case took almost 9 hours to be completed on the CPU, meanwhile it was completed on the GPU server in less than 8 minutes, achieving a speedup of 70. The desktop computer

was a bit faster with an speedup of nearly 78, while the laptop computer, despite its limitations, was able to finish the simulation in less than 14 minutes (38 times faster than CPU). Even though the laptop was slower than the other two GPU configurations, the performance achieved in such a small form factor is remarkable. In terms of throughput, the CPU configuration shows similar values to T2, because the presence of dry elements is similar in both tests, and both include a single class of soil particles, indicating similar computing cost per cell on average. However, in the case of GPU the throughput was higher than in T2 (due to the bigger mesh) and T3 (due to more dry elements and less soil particle classes).

6 CONCLUSIONS

We presented the implementation of a new fully distributed multiclass soil erosion module in the software package Iber+, which solves the 2D shallow water equations. The model considers the transport of sediment particles of different size by overland flow, due to bed load and suspended load. The rainfall-driven and runoff-driven erosion processes are considered independently as the source terms for the suspended load transport equation, using for that purpose physically-based formulations that have been proposed, validated and published in previous experimental studies. A mass conservation equation is solved for each sediment class, in order to compute the evolution of the mass of sediment particles in the soil layer.

The model can be used to analyse soil erosion and sediment transport by overland flow at spatial scales ranging from laboratory experiments to meso-scale catchments, with spatial discretisations ranging from a few cm (at small spatial scales) to several m (at the catchment scale). At the laboratory scale in test case T1, the model has proven to be a potential tool to analyse size-selectivity processes. It can also be used to analyse soil erosion at the hillslope scale, as shown in test case T2. At the basin scale (test case T3), the GPU-enhanced implementation of the model is able to simulate the erosion generated in a meso-scale catchment by rainfall events of several hours in a few minutes, using a numerical mesh of circa 10^5 mesh elements. It can also be used to analyse bed load transport and flow driven erosion processes at the river reach scale, as shown in test case T4.

In terms of computational performance, the throughput of the GPU implementation (number of mesh elements processed per second) is highly dependent on the number of sediment classes, the number of mesh elements and the relative extension of dry zones in the domain. The throughput decreases as the number of sediment classes increases, because more equations need to be solved. The throughput increases with the number of mesh elements, because the GPU parallelism is more efficiently exploited through HPC techniques. The extension of dry zones also has an impact on the throughput, since the number of mathematical operations to be performed in the dry elements is much lower than in the wet elements. For these reasons it is not possible to give an overall quantification of the throughput. For instance, in the desktop configuration used in this work (Nvidia RTX 3080 ti) the throughput varied from 0.27 MCells/s in test case T1 (very low number of mesh elements, seven size classes and no dry regions) to 141 MCells/s in test case T4 (large number of mesh elements, one single size class and several dry regions). On the CPU sequential implementation the throughput is much lower varying between 0.18 MCells/s in test case T1 to 1.8 MCells/s in test case T4. Thus, the speed-ups achieved with the GPU implementation can reach two orders of magnitude in problems with around 50k-100k mesh elements using a Nvidia RTX 3080 in a standard desktop.

Future work should be directed to the application of the model to the analysis of different kinds of soil erosion processes. For that purpose, the model is freely available to the scientific community, and can be downloaded within the software package Iber from `www.iberaula.com`.

Open Research Section

The Iber+ software used to perfom the computation showed in this paper, as well as the four test cases and the related data are all openly and permanently available at `https://entrepot.recherche.data.gouv.fr/dataverse/soilsedimentmodellingdata`.

Acknowledgments

O.G.-F. was funded by the Spanish Ministerio de Universidades under application 33.50.460A.752, by the European Union NextGenerationEU/PRTR through a contract Margarita Salas from the University of Vigo, by the IGE lab and by the French Ministry of Environment (Direction Générale de la Prévention des Risques Ministère de la Transition Ecologique et Solidaire) within the multirisk agreement SRNH-IRSTEA 2020 (Action TorRex). G.N.

and C.L. were supported by the Labex OSUG@2020 (Investissements d'Avenir, grant agreement ANR-10-LABX-0056). G.P. was supported by the LabEx Tec21 (Investissements d'avenir - grant agreement n°ANR-11-LABX-0030). Some of the computations presented in this paper were performed using the GRICAD high performance infrastructure (https://gricad.univ-grenoble-alpes.fr), which is supported by the Rhône-Alpes region (GRANT CPER07_13 CIRA) and the Equip@Meso project (Investissements d'avenir - grant agreement n° ANR-10-EQPX-29-01).

References

Baldock, T. E., Tomkins, M. R., Nielsen, P., & Hughes, M. G. (2004). Settling velocity of sediments at high concentrations. *Coastal engineering*, *51*(1), 91-100.

Belikov, E., Deligiannis, P., Totoo, P., Aljabri, M., & Loidl, H.-W. (2013). *A survey of high-level parallel programming models.* Heriot-Watt University. Retrieved from `http://www.macs.hw.ac.uk/cs/techreps/docs/files/HW-MACS-TR-0103.pdf`

Beuselinck, L., Govers, G., Hairsine, P. B., Sander, G. C., & Breynaert, M. (2002). The influence of rainfall on sediment transport by overland flow over areas of net deposition. *Journal of Hydrology*, *257*, 145-163.

Beuselinck, L., Govers, G., Steegen, A., Hairsine, P. B., & Poesen, J. (1999). Evaluation of the simple settling theory for predicting sediment deposition by overland flow. *Earth Surface Processes and Landforms*, *24*, 993-1007.

Beven, K. (2006). A manifesto for the equifinality thesis. *Journal of hydrology*, *320*(1-2), 18–36.

Bladé, E., Cea, L., Corestein, G., Escolano, E., Puertas, J., Vázquez-Cendó, E., ... Coll, A. (2014). Iber: herramienta de simulación numérica del flujo en ríos. *Revista internacional de métodos numéricos para cálculo y diseño en ingeniería*, *30*(1), 1-10.

Boudevillain, B., Delrieu, G., Galabertier, B., Bonnifait, L., Bouilloud, L., Kirstetter, P. E., & Mosini, M. L. (2011). The cévennes-vivarais mediterranean hydrometeorological observatory database. *Water Resources Research*, *47*(7).

Brufau, P., García-Navarro, P., & Vázquez-Cendón, M. E. (2004). Zero mass error using unsteady wetting-drying conditions shallow flows over dry of irregular topography. *Int. J. Numer. Meth. Fluids*, *45*, 1047-1082.

Carrega, P., & Michelot, N. (2021, January). Une catastrophe hors norme d'origine météorologique le 2 octobre 2020 dans les montagnes des Alpes-Maritimes. *Physio-Géo*(Volume 16), 1–70. doi: 10.4000/physio-geo.12370

Cea, L., Alvarez, M., & Puertas, J. (2022). Estimation of flood-exposed population in data-scarce regions combining satellite imagery and high resolution hydrological-hydraulic modelling: A case study in the licungo basin (mozambique). *Journal of Hydrology: Regional Studies*, *44*, 101247.

Cea, L., & Bladé, E. (2015). A simple and efficient unstructured finite volume scheme for solving the shallow water equations in overland flow applications. *Water Resources Research*, *51*(7), 5464-5486.

Cea, L., Garrido, M., & Puertas, J. (2010). Experimental validation of two-dimensional depth-averaged models for forecasting rainfall-runoff from precipitation data in urban areas. *Journal of Hydrology*, *382*, 88-102.

Cea, L., Legout, C., Darboux, F., Esteves, M., & Nord, G. (2014). Experimental validation of a 2D overland flow model using high resolution water depth and velocity data. *Journal of Hydrology*, *513*, 142-153.

Cea, L., Legout, C., Grangeon, T., & Nord, G. (2016). Impact of model simplifications on soil erosion predictions: application of the glue methodology to a distributed event-based model at the hillslope scale. *Hydrological Processes*, *30*(7), 1096-1113.

Cea, L., Puertas, J., & Vázquez-Cendón, M. E. (2007). Depth averaged modelling of turbulent shallow water flow with wet-dry fronts. *Archives of Computational Methods in Engineering (ARCME)*, *14*(3).

Cea, L., & Vázquez-Cendón, M. E. (2012). Unstructured finite volume discretisation of bed friction and convective flux in solute transport models linked to the shallow water equations. *Journal of Computational Physics*, *231*, 3317-3339.

Church, M., & Jakob, M. (2020, August). What Is a Debris Flood? *Water Resources Research*, *56*(8). doi: 10.1029/2020WR027144

Costabile, P., & Costanzo, C. (2021). A 2d-swes framework for efficient catchment-scale simulations: Hydrodynamic scaling properties of river networks and implications for non-uniform grids generation. *Journal of Hydrology*, *599*, 126306.

Domínguez, J. M., Fourtakas, G., Altomare, C., Canelas, R. B., Tafuni, A., García-

Feal, O., ... Gómez-Gesteira, M. (2021, 3). Dualsphysics: from fluid dynamics to multiphysics problems. *Computational Particle Mechanics*. doi: 10.1007/s40571-021-00404-2

Echeverribar, I., Morales-Hernández, M., Brufau, P., & García-Navarro, P. (2019). 2d numerical simulation of unsteady flows for large scale floods prediction in real time. *Advances in Water Resources*, *134*, 103444.

Esteves, M., Legout, C., Navratil, O., & Evrard, O. (2019). Medium term high frequency observation of discharges and suspended sediment in a mediterranean mountainous catchment. *Journal of Hydrology*, *568*, 562-574.

Ferraro, D., Costabile, P., Costanzo, C., Petaccia, G., & Macchione, F. (2020). A spectral analysis approach for the a priori generation of computational grids in the 2-d hydrodynamic-based runoff simulations at a basin scale. *Journal of Hydrology*, *582*, 124508.

Foster, G. R., Flanagan, D. C., Nearing, M. A., Lane, L. J., Risse, L. M., & Finkner, S. C. (1995). Water erosion prediction project: Hillslope profile and watershed model documentation. In D. Flanagan & M. Nearing (Eds.), (chap. Hillslope erosion component). USDA-ARS National Soil Erosion Research Laboratory, West Lafayette, Indiana.

Gao, B., Walter, M. T., Steenhuis, T. S., Parlange, J. Y., Nakano, K., Hogarth, W. L., & Rose, C. W. (2003). Investigating ponding depth and soil detachability for a mechanistic erosion model using a simple experiment. *Journal of Hydrology*, *277*(1-2), 116-124.

Garcia, M. H. (2006). *Sedimentation engineering: Processes, measurements, modeling, and practice*. Reston, Virginia: ASCE.

García-Alén, G., González-Cao, J., Fernández-Nóvoa, D., Gómez-Gesteira, M., Cea, L., & Puertas, J. (2022). Analysis of two sources of variability of basin outflow hydrographs computed with the 2d shallow water model iber: Digital terrain model and unstructured mesh size. *Journal of Hydrology*, *612*, 128182.

García-Feal, O., González-Cao, J., Gómez-Gesteira, M., Cea, L., Domínguez, J. M., & Formella, A. (2018). An accelerated tool for flood modelling based on iber. *Water*, *10*(10), 1459.

García-Feal, O., Cea, L., González-Cao, J., Manuel Domínguez, J., & Gómez-Gesteira, M. (2020, 2). Iberwq: A gpu accelerated tool for 2d water

quality modeling in rivers and estuaries. *Water*, *12*, 413. Retrieved from https://www.mdpi.com/2073-4441/12/2/413 doi: 10.3390/w12020413

Garland, M., Grand, S. L., Nickolls, J., Anderson, J., Hardwick, J., Morton, S., ... Volkov, V. (2008, 7). Parallel computing experiences with cuda. *IEEE Micro*, *28*, 13-27. doi: 10.1109/MM.2008.57

Govers, G. (1992). Overland flow, hydraulics and erosion mechanics. In A. Parsons & A. Abrahams (Eds.), (chap. Evaluation of transporting capacity formulae for overland flow). University College London Press.

Grand, S. L., Götz, A. W., & Walker, R. C. (2013, 2). Spfp: Speed without compromise—a mixed precision model for gpu accelerated molecular dynamics simulations. *Computer Physics Communications*, *184*, 374-380. Retrieved from https://linkinghub.elsevier.com/retrieve/pii/S0010465512003098 doi: 10.1016/j.cpc.2012.09.022

Grangeon, T. (2012). *Etude multi-échelle de la granulométrie des particules fines générées par érosion hydrique: apports pour la modélisation* (Unpublished doctoral dissertation). Université de Grenoble.

Hairsine, P. B., & Rose, C. W. (1992a). Modeling water erosion due to overland-flow using physical principles. 1. sheet flow. *Water Resources Research*, *28*(1), 237-243.

Hairsine, P. B., & Rose, C. W. (1992b). Modeling water erosion due to overland-flow using physical principles. 2. rill flow. *Water Resources Research*, *28*(1), 245-250.

Heng, B. C. P., Sander, G. C., Armstrong, A., Quinton, J. N., Chandler, J. H., & Scott, C. F. (2011). Modeling the dynamics of soil erosion and size-selective sediment transport over nonuniform topography in flume-scale experiments. *Water Resources Research*, *47*(2), W02513.

Hong, Y., Bonhomme, C., Le, M. H., & Chebbo, G. (2016). A new approach of monitoring and physically-based modelling to investigate urban wash-off process on a road catchment near paris. *Water Research*, *102*, 96-108.

Jakob, M., Davidson, S., Bullard, G., Busslinger, M., Collier-Pandya, B., Grover, P., & Lau, C. (2022, April). Debris-Flood Hazard Assessments in Steep Streams. *Water Resources Research*, *58*(4). doi: 10.1029/2021WR030907

Jomaa, S., Barry, D. A., Brovelli, A., Sander, G. C., Parlange, J. Y., Heng, B. C. P.,

& van Meerveld, H. J. T. (2010). Effect of raindrop splash and transversal width on soil erosion: Laboratory flume experiments and analysis with the hairsine-rose model. *Journal of Hydrology*, *395*, 117-132.

Kawanisi, K., & Shiozaki, R. (2008). Turbulent effects on the settling velocity of suspended sediment. *Journal of hydraulic engineering*, *134*(2), 261-266.

Kinnell, P. I. A. (1990). The mechanics of raindrop induced flow transport. *Australian Journal of Soil Research*, *28*, 497-516.

Kinnell, P. I. A. (2005). Raindrop-impact-induced erosion processes and prediction: a review. *Hydrological Processes*, *19*, 2815-2844.

Legout, C., Freche, G., Biron, R., Esteves, M., Navratil, O., Nord, G., ... others (2021). A critical zone observatory dedicated to suspended sediment transport: the meso-scale galabre catchment (southern french alps). *Hydrological Processes*, *35*(3), e14084.

Legout, C., Poulenard, J., Nemery, J., Navratil, O., Grangeon, T., Evrard, O., & Esteves, M. (2013). Quantifying suspended sediment sources during runoff events in headwater catchments using spectrocolorimetry. *Journal of Soils and Sediments*, *13*(8), 1478-1492.

LeVeque, R. J. (2002). *Finite volume methods for hyperbolic problems* (Vol. 31). Cambridge University Press.

Li, R. M. (1979). Modeling in rivers. In H. W. Shen (Ed.), (chap. Water and sediment routing from watershed). Wiley, New-York.

Merrill, D. (2013). *Cub: Cuda unbound.* Retrieved from `https://nvlabs.github.io/cub/`

Michalakes, J., & Vachharajani, M. (2008, 12). Gpu acceleration of numerical weather prediction. *Parallel Processing Letters*, *18*, 531-548. doi: 10.1142/S0129626408003557

Morales-Hernández, M., Sharif, M. B., Kalyanapu, A., Ghafoor, S. K., Dullo, T. T., Gangrade, S., ... Evans, K. J. (2021). Triton: A multi-gpu open source 2d hydrodynamic flood model. *Environmental Modelling & Software*, *141*, 105034.

Mügler, C., Planchon, O., Patin, J., Weill, S., Silvera, N., Richard, P., & Mouche, E. (2011). Comparison of roughness models to simulate overland flow and tracer transport experiments under simulated rainfall at plot scale. *Journal of Hydrology*, *402*, 25-40.

Naves, J., Rieckermann, J., Cea, L., Puertas, J., & Anta, J. (2020). Global and local sensitivity analysis to improve the understanding of physically-based urban wash-off models from high-resolution laboratory experiments. *Science of the Total Environment*, *709*, 136152.

Nord, G., Boudevillain, B., Berne, A., Branger, F., Braud, I., Dramais, G., ... others (2017). A high space–time resolution dataset linking meteorological forcing and hydro-sedimentary response in a mesoscale mediterranean catchment (auzon) of the ardèche region, france. *Earth System Science Data*, *9*(1), 221–249.

Nord, G., & Esteves, M. (2005). PSEM 2D: A physically based model of erosion processes at the plot scale. *Water Resources Research*, *41*(W08407).

Nord, G., & Esteves, M. (2007). Evaluation of sediment transport formulae and detachment parameters in eroding rills using PSEM2D and the Water Erosion Prediction Project (WEPP) database. *Water Resources Research*, *43*(W08420), 1-14.

NVIDIA. (2023). *Cuda c++ programming guide.* Retrieved from `https://docs.nvidia.com/cuda/pdf/CUDA_C_Programming_Guide.pdf`

Ouyang, C., Xiang, W., An, H., Wang, F., Yang, W., & Fan, J. (2023). Mechanistic analysis and numerical simulation of the 2021 post-fire debris flow in xiangjiao catchment, china. *Journal of Geophysical Research: Earth Surface*, *128*(1), e2022JF006846.

Pasquero, C., Provenzale, A., & Spiegel, E. A. (2003). Suspension and fall of heavy particles in random two-dimensional flow. *Physical review letters*, *91*(5), 054502.

Payrastre, O., Nicolle, P., Bonnifait, L., Brigode, P., Astagneau, P., Baise, A., ... Sevrez, D. (2022, June). Tempête Alex du 2 octobre 2020 dans les Alpes-Maritimes : une contribution de la communauté scientifique à l'estimation des débits de pointe des crues. *LHB*, 2082891. doi: 10.1080/27678490.2022.2082891

Piton, G., & Recking, A. (2019, August). Steep Bedload-Laden Flows: Near Critical? *Journal of Geophysical Research: Earth Surface*, *124*(8), 2160–2175. doi: 10.1029/2019JF005021

Piton, G., & Rodier, R. (2022). *Comparaison des outils de modélisation des évolutions du fond par charriage - Analyse du potentiel et des limitations des*

outils de modélisation 2D sur deux cas d'étude (Tech. Rep.). INRAE ETNA; DGPR (Direction Générale de la Prévention des Risques - Ministère de la Transition Ecologique et Solidaire). Retrieved from `https://hal.inrae.fr/hal-03735959v1`

Poulenard, J., Legout, C., Nemery, J., Bramorski, J., Navratil, O., Douchin, A., ... Esteves, M. (2012). Tracing sediment sources during floods using diffuse reflectance infrared fourier transform spectrometry (drifts): A case study in a highly erosive mountainous catchment (southern french alps). *Journal of Hydrology*, *414*, 452-462.

Sanz-Ramos, M., Bladé, E., González-Escalona, F., Olivares, G., & Aragón-Hernández, J. L. (2021). Interpreting the manning roughness coefficient in overland flow simulations with coupled hydrological-hydraulic distributed models. *Water*, *13*(23), 3433.

Sharma, P. P., Gupta, S. C., & Foster, G. R. (1993). Predicting soil detachment by raindrops. *Soil Science Society of America Journal*, *57*, 674-680.

Sharma, P. P., Gupta, S. C., & Foster, G. R. (1995). Raindrop-induced soil detachment and sediment transport from interrill areas. *Soil Science Society of America Journal*, *59*, 727-734.

Shaw, S. B., Parlange, J. Y., Lebowitz, M., & Walter, M. T. (2009). Accounting for surface roughness in a physically-based urban wash-off model. *Journal of Hydrology*, *367*, 79-85.

Shaw, S. B., Walter, M. T., & Steenhuis, T. S. (2006). A physical model of particulate wash-off from rough impervious surfaces. *Journal of Hydrology*, *327*, 618-626.

Sun, Y., Bohm Agostini, N., Dong, S., & Kaeli, D. (2019, 11). Summarizing cpu and gpu design trends with product data. *arXiv preprint arXiv:1911.11313*. Retrieved from `http://arxiv.org/abs/1911.11313`

Sutter, H. (2005). The free lunch is over: A fundamental turn toward concurrency in software. *Dr. Dobb's Journal*, *30*, 1-9. Retrieved from `http://www.mscs.mu.edu/~rge/cosc2200/homework-fall2013/Readings/FreeLunchIsOver.pdf`

Sutter, H., & Larus, J. (2005). Software and the concurrency revolution. *Queue*, *3*, 54-62. Retrieved from `https://doi.org/10.1145/1095408.1095421` doi: 10.1145/1095408.1095421

Tatard, L., Planchon, O., Wainwright, J., Nord, G., Favis-Mortlock, D., Silvera, N., ... Huang, C. H. (2008). Measurement and modelling of high-resolution flow-velocity data under simulated rainfall on a low-slope sandy soil. *Journal of Hydrology*, *348*(1-2), 1 - 12.

Toro, E. F. (2001). *Shock-capturing methods for free-surface shallow flows.* Chichester, West Sussex PO19 1UD, England: Wiley.

Toro, E. F. (2009). *Riemann solvers and numerical methods for fluid dynamics: A practical introduction.* New York: Springer-Verlag.

Tromp-van Meerveld, H., Parlange, J.-Y., Barry, D. A., Tromp, M., Sander, G. C., Walter, M. T., & Parlange, M. B. (2008). Influence of sediment settling velocity on mechanistic soil erosion modeling. *Water Resources Research*, *44*(6), W06401. doi: 10.1029/2007WR006361

Uber, M., Nord, G., Legout, C., & Cea, L. (2021). How do modeling choices and erosion zone locations impact the representation of connectivity and the dynamics of suspended sediments in a multi-source soil erosion model? *Earth Surface Dynamics*, *9*(1), 123-144.

van Rijn, L. C. (1984). Sediment transport, Part II: Suspended load transport. *J. Hydraul. Eng.*, *110*(11), 1613-1641.

Vrugt, J. A., Ter Braak, C. J. F., Hoshin, G. V., & Robinson, B. A. (2009). Equifinality of formal (dream) and informal (glue) bayesian approaches in hydrologic modeling? *Stochastic environmental research and risk assessment*, *23*(7), 1011–1026.

Xilin, X., Qiuhua, L., & Xiaodong, M. (2019). A full-scale fluvial flood modelling framework based on a high-performance integrated hydrodynamic modelling system (HiPIMS). *Advances in Water Resources*, *132*, 103392.